

MATHEMATICAL DERIVATION OF FLUORESCENCE RECOVERY AFTER
PHOTOBLEACHING MODELS

A Thesis

by

JEDIDIAH KOOMSON

Submitted to the Office of Graduate Studies
of Texas A&M University-Commerce
in partial fulfillment of the requirements
for the degree of
MASTER OF SCIENCE
May 2018

ProQuest Number: 10812516

All rights reserved

INFORMATION TO ALL USERS

The quality of this reproduction is dependent upon the quality of the copy submitted.

In the unlikely event that the author did not send a complete manuscript and there are missing pages, these will be noted. Also, if material had to be removed, a note will indicate the deletion.



ProQuest 10812516

Published by ProQuest LLC (2018). Copyright of the Dissertation is held by the Author.

All rights reserved.

This work is protected against unauthorized copying under Title 17, United States Code
Microform Edition © ProQuest LLC.

ProQuest LLC.
789 East Eisenhower Parkway
P.O. Box 1346
Ann Arbor, MI 48106 – 1346

MATHEMATICAL DERIVATION OF FLUORESCENCE RECOVERY AFTER
PHOTOBLEACHING MODELS

A Thesis

by

JEDIDIAH KOOMSON

Approved by:

Advisor: Minchul Kang

Committee: Pamela Webster
Thomas Boucher
Yelin Ou

Head of Department: Tingxiu Wang

Dean of the College: Brent Donham

Dean of Graduate Studies: Matthew A. Wood

Copyright © 2018

Jedidiah Koomson

ABSTRACT

MATHEMATICAL DERIVATION OF FLUORESCENCE RECOVERY AFTER
PHOTOBLEACHING MODELS

Jedidiah Koomson, MS
Texas A&M University-Commerce, 2018

Advisor: Minchul Kang, PhD

Fluorescence recovery after photobleaching (FRAP) is a laser microscopy technique extensively used to determine kinetic properties of cells using fluorophores. FRAP is based on irreversibly bleaching a set of proteins tagged with green fluorescent protein (GFP) in a region of interest and monitoring the recovery in fluorescence due to diffusion of surrounding intact probes into the bleached spot. FRAP is being widely used in many areas of biology to measure molecular transport and diffusion in comparison with mathematical models derived for specific domains. This study focused on deriving mathematical models of FRAP for various geometries and conditions depending on their locations in the cell, creating a database, and constructing a mathematical model with the help of MATLAB. FRAP models for pure diffusion for various geometries in 1~2 spatial dimensions with different boundary conditions, which are applicable to both conventional and confocal FRAP, was considered. For a circular bleaching spot, the geometries considered were infinite line, finite interval, a circle, infinite plane, sphere, and infinite three-dimensional space for reflective and restrictive boundary conditions if applicable.

Finally, future directions are proposed to focus on interesting ways to apply this new model in vivo.

ACKNOWLEDGEMENTS

My greatest thanks go to the Almighty God. This work would not have been possible without the help and support of many people. I would like to specifically thank my thesis supervisor, Dr. Minchul Kang, who was very patient and supporting, especially with the creative ideas and discussions whilst deriving the models. I would also like to thank my thesis committee members for accepting this responsibility of guiding me through these semesters. Special thanks go to my family members. Their prayers and support were very much appreciated. To my colleagues in TAMUC who sometimes helped me in my derivations, I say thank you. I also acknowledge the financial support of Texas A&M University-Commerce.

TABLE OF CONTENTS

ABSTRACT	iv
ACKNOWLEDGEMENTS	vi
LIST OF FIGURES	x
CHAPTER	
1. INTRODUCTION	1
Overview	1
Limitations	4
2. BASICS OF FRAP	6
Biological Basics	6
Nuclear Protein	6
Architecture of the Nucleus	6
Dynamic Properties.....	7
Green Fluorescence Protein (GFP)	8
Experimental Basics.....	9
Fluorescence and Photobleaching.....	9
Absorption-Emission Cycle	11
Confocal Laser Scanning Microscope (CLSM).....	12
Breakdown of CLSM Components.....	14
Acousto-Optic Tunable Filter	15
Qualitative FRAP	15
Principles of FRAP	15
Fluorophores Used in FRAP.....	16

CHAPTER

Quantitative FRAP	16
Normalizing FRAP Data.....	196
Laser Profile.....	17
Biophysical Properties	17
MATHEMATICAL MODEL.....	18
Diffusion Modelling.....	18
Diffusion Coefficient	19
Boundary Conditions	20
Dirichlet boundary conditions.....	200
Neumann boundary conditions	21
Recovery Curve	21
Numerical Solution	22
Analytic Solution	22
3. METHODOLOGY & ANALYSIS	24
Summary of Steps to Perform Experiment	26
Mathematical Derivation	26
FRAP models for pure diffusion in 1D (\mathbb{R}).....	26
FRAP models for pure diffusion in 2D (\mathbb{R}^2).....	29
FRAP models for pure diffusion in nD (\mathbb{R}^N)	32
FRAP models on $[-1,1]$ with reflective boundaries (Neumann Boundary Conditions).....	35
FRAP models on a circle S^1	37

CHAPTER

FRAP models on a Disk \mathbb{D}^2	40
FRAP model on a sphere (\mathbb{S}^2)	40
Coding Results and Graph	48
Algorithm for \mathbb{R}^1 Model.....	48
Algorithm for \mathbb{R}^2 and \mathbb{R}^N Model	49
Algorithm for Finite Interval Model using Neumann Boundary Condition.....	49
Algorithm for Finite Interval Model using Dirichlet Boundary Condition.....	51
Algorithm for Disk Model using Neumann Boundary Condition	52
4. CONCLUSION.....	54
REFERENCES	56
APPENDIX.....	63
Matlab codes for FRAP models.....	64
VITA	67

LIST OF FIGURES

FIGURE

1. Cross section of a nuclear pore and Nucleus of a cell. Adapted from [37]	8
2. Protein backbone structure of GFP. Extracted from [2]	9
3. GFP Spectra of an enhanced GFP (adapted from [3])	10
4. A modified Jablonski Diagram	11
5. Setup of a ConfoCor2 (Zeiss)	13
6. Pictorial view of spherical coordinates.....	44
7. 1D FRAP Recovery Curve.....	48
8. FRAP Recovery Curve in \mathbb{R}^2	49
9. FRAP curve of a finite domain with Neumann boundary condition	50
10. FRAP curve of a finite domain with Dirichlet boundary condition.....	52
11. FRAP curve of a disk with Neumann boundary condition.....	53

Chapter 1

INTRODUCTION

Overview

Reaction diffusion is a very common but essential process in biological life. Diffusivity is important in determining the time and space scales of cellular events. In order to determine the kinetic rate constants like diffusion coefficients, researchers needed to understand how proteins in the cell behave and work. To this purpose, fluorescence recovery after photobleaching (FRAP) was invented to determine the kinetics in diffusion of biomolecules in cells. FRAP is a fluorescence microscopy technique just like fluorescence localization in photobleaching (FLIP), fluorescence resonance energy transfer (FRET), fluorescence localization after photobleaching (FLAP), and fluorescence lifetime image microscopy (FLIM) that are used to measure both molecular diffusion and transport. For example, fluorescence microscopy can be used to study how certain antibodies and disease conditions or impurities in inorganic material work. Due to fluorescence probes, FRAP has been a valuable technique used in many biological research fields. These fluorescent probes emit lights at various wavelengths when excited by dissipating excess energy. Fluorescence microscopy has gained a lot of ground in most medical and biological fields because it has enabled researchers to identify cells and their components with a high degree of specificity. These experiments, in conjunction with kinetic modelling, have helped researchers assess the binding rates and diffusion constants.

First developed in 1904 by August Kohler at the Zeiss Optical Laboratory in Jena, Germany, fluorescence microscopy was performed using a cadmium arc lamp as his source of light [1]. This was later improved by Oskar Heimstadt in 1911. At that time and even nowadays, these microscopes had many drawbacks. Philipp Elinger and August Hirt later invented the epi-

fluorescence microscope in 1929, which helped solved most of the problems of effective separation of fluorescence signal from the excitation light. Gould, Townes, Schawlow, and Maiman [2], [3] later developed lasers to solve the problem of inadequate power to excite the fluorophores to high wavelengths. This was principled on Einstein's theoretical foundations on simulated emission [4].

Advancement in fluorescence microscopy will be understated without acknowledging the invention of the commercial laser scanning confocal microscopes (LSCMs) and the discovery of green fluorescent proteins (GFPs) in the 1990s [5]-[9]. It has made FRAP accessible and extended it to other protein dynamics [10], [11]-[13]. GFP can be found in the photo-organs of some species of jellyfish, *Aequorea victoria*. The general public mistake the glow of jellyfishes in pictures; instead, the glow occurs due to the reflection of the flash used to photograph the jellyfish. Many more fluorescence proteins, like *Anemonia majano* (AmCyan1) and *Discosoma* (DsRed), have been identified, resulting in a wide color palette for different biological experiments.

One of the first documented uses of FRAP was in the 1970s [14], [15] for checking the lateral diffusion of proteins tagged with fluorophores at the plasma membrane, such as diffusion on a sphere and diffusion in an infinite plane, with the assumption that the bleaching spot is small in size. This made computations easier. Then came the conventional FRAP using the static laser beam, which was an improvement on Axelrod's work by Soumpasis [16]. LSCM was first used in FRAP modelling by Blonk et al. [17] with their assumption that a stationary laser is used in the photobleaching phase whilst a laser line-scanner is used in the fluorescence recovery phase. Braeckmans et al. [18] mathematically modeled photobleaching using the laser line scanning technique after Wedekind et al. [19] introduced it. They assumed that the bleaching

stage occurs faster than the diffusion stage and no information about the distribution of bleached molecules outside the bleached spot is required for its analysis. However, these assumptions might not be true for confocal FRAP experiments because, when using a single scanning laser for soluble proteins, bleaching and imaging occurs along with significant amounts of diffusion in the LSCM.

There has been some advancement in variations of confocal FRAP that made it easy to photobleach spots of different geometries, including size and shape, determined by the user, which allows the user to bleach specific regions in order to monitor protein dynamics within and between individual subcellular compartments. The user can do the same in FLIP, inverse FRAP, and selective photobleaching [20], [21].

FRAP needed a bounded and known bleach distribution. It was therefore restricted to thin samples like cell membranes and a known disk-shaped bleaching distribution [22] because an unbounded double-cone shape of the fluorescence excitation profile caused problems. Berk proposed using FRAP with spatial Fourier analysis so that FRAP can be used on thicker and 3D samples [23]. To determine the coefficient of diffusion using this method, all researchers need is to measure the decay of several spatial frequencies to the spatial Fourier transform. It is not required to know the initial bleached fluorophore spatial distribution. With all said, apart from models based on spheres [14] and reaction diffusion in finite 2D and 3D domains [24], [25], most FRAP models are still based on an infinite plane's \mathbb{R}^2 diffusion equation.

This study not only developed a FRAP formalism to compensate for diffusion during photobleaching, it also incorporated geometries of the subjects in the models [26]-[28]. Some of these relevant geometries are used in many applications of biology:

i) the infinite line (\mathbb{R}^1)

v) a sphere (\mathbb{S}^2)

- ii) a finite interval $([-l; l])$
- iii) a circle (\mathbb{S}^1)
- iv) an infinite plane (\mathbb{R}^2)
- vi) an infinite dimensional space (\mathbb{R}^N)
- vii) a disk

These geometries are important because FRAP models are dependent on the organelle's geometry. For an abnormal-shaped mitochondria [29], ring-shaped lysosomes in monocytes [30], and ring-shaped micro tubular structures [31], the FRAP model is based on that of a circle (\mathbb{S}^1) . FRAP models based on circles and disks can be used for protein kinetics in cases where circular shaped cells intersect with a confocal plane. Lastly, the FRAP models of spheres \mathbb{S}^2 based on the local curvature of the cell membrane must be considered.

The Neumann and Dirichlet boundary conditions were considered if diffusion is blocked by the boundaries and if the concentration of the fluorescence molecules is constant at the boundaries, respectively. One advantage of using a static laser over a scanning laser is that the latter takes more time compared to a static laser, which allows significant diffusion during the bleaching process [32].

Limitations

This study had the following constrains:

- Due to the movement of living cells during experiments, the modeling and recovery data might be slightly wrong unless an alignment algorithm is taken into consideration.
- Soluble and bound proteins were assumed to be mobile.
- Diffusion during the bleach period was not accounted for, thereby underestimating diffusion coefficients.

- The experimental model is not associated with the 2-dimensional model. Thus, when bleaching 3-dimensional samples, fluorophores below and on top of the focal plane were photobleached. Researchers can assume a bleach volume of cone shape if the objectives of the microscope have a low numerical aperture.
- Sometimes the bleach structure is very complex to be visible in the focal plane when objectives have high numerical aperture.
- To guarantee full recovery after bleaching, it was assumed that for most FRAP curve data, the region of interest (ROI) size was smaller than for the subject under study. However, the data gets very noisy if the ROI size is too small.
- A low number of fluorophores in an ROI means a higher intensity for a sufficient signal. Researchers might obtain incorrect FRAP results when trying to correct the immobile fraction. This is because the immobile fraction contributes more significantly to the loss in fluorescence than that of the mobile fraction.
- Reversible photobleaching or fluorophore blinking may result in an inaccurate FRAP result.
- It was assumed that the fluorophores recover into the focal volume by diffusion only.

Chapter 2

BASICS OF FRAP

Biological Basics

FRAP experiments mostly are done in the biological fields. In this section, few details on biological cell structures and protein dynamics are given to provide a better understanding of how FRAP experiments are performed. Lastly, I deal with how mathematical models were derived from protein dynamics during these experiments.

Nuclear Protein

Most functions performed by cells are due to proteins. The study of functional genomics, that is, protein function, and nuclear organization was necessary after the entire genome was sequenced. Researchers need to know the physical properties of the nucleus gene compartments and the functions they performed. RNA processing, DNA replication, transcription, and repairs are important processes that need to be studied.

The nucleus of a cell defines the eukaryotes. Inside it is the DNA in the compacted form of chromatin. For a long time, the nucleus had been assumed to be gel-like; thus, active transportation of protein within the nucleus is required since movement is restricted. Such an assumption was nullified with the development of GFP in the 1990s by Tsien, Chalfie, and Shimomura [6]-[9], [33]. Through this discovery, it is now possible to find the biophysical properties of nuclear proteins without causing changes to the cell.

Architecture of the Nucleus

The largest of the cellular compartments in a cell is the nucleus, which averages in diameter from 10 to 20 mm and contains chromosomes with most of genome as well as multiple parts needed in genetics. The nuclear envelope has a doubled membrane that creates a boundary

between the cytoplasm and the nuclear space. There are also nuclear pores embedded in the nuclear envelope which form routes that allow the transportation of molecules in regulated forms from the cytoplasm to the nucleus for nuclear-cytoplasmic exchange [34]. Chromatins are complex DNA-proteins present in the nucleus. Ribosomes are created by the nucleolus to build protein from the set of genetic instructions. Proteins are exchanged continuously between each compartment and the nucleoplasm, thus becoming steady-state structures. Proteins have a stay time in their compartment of about a minute or maybe less. The ratio of influx and efflux of proteins helps identify the morphology of a compartment, causing the structures to have high internal dynamics.

Dynamic Properties

Made aware of the fact that most proteins are very mobile inside the nucleus, their movement is still independent from adenosine triphosphate (ATP) and therefore not slowed down by lower temperatures. This verifies the movement of protein as non-directional and diffusion-based; thus, it is an efficient mode of transportation that ensures proteins are everywhere in the nucleus [35], [36]. However, researchers face a difficult task of predicting the possible conformations to which protein complexes can adopt. Mostly determined by their amino acid sequences, they can transition into different states.

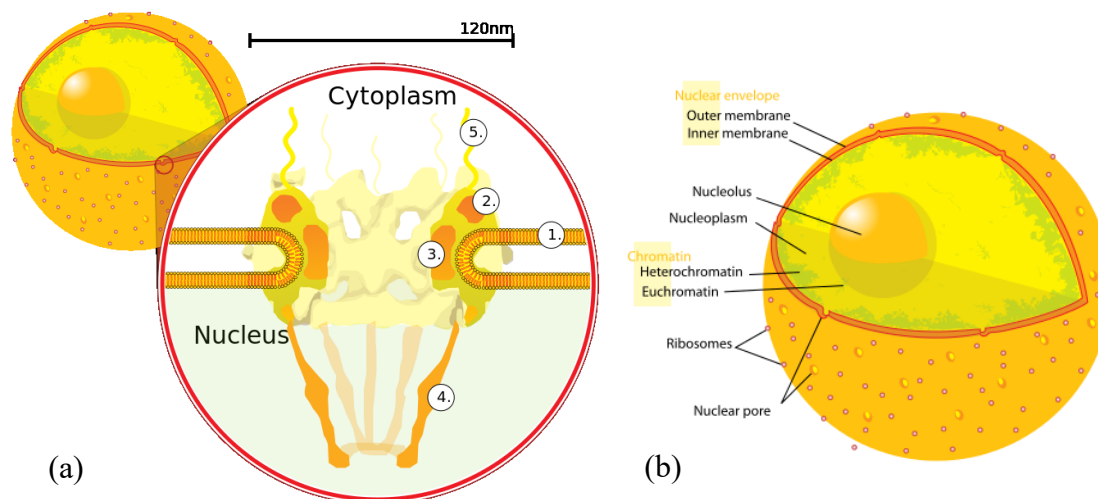


Fig. 1. Cross section of a nuclear pore and Nucleus of a cell. Adapted from [37]. (a) The numbered parts of the diagram are as follows: (1) Nuclear envelope (2), the outer ring, (3) spokes, (4) basket, and (5) filaments. (b) The eukaryotic cell nucleus in the diagram shows three ribosome-studded, double membranes of the nuclear envelope, the DNA (complexed as chromatin), and the nucleolus and the nucleoplasm.

Green Fluorescence Protein (GFP)

Composed of a rigid single-protein chain with a unique molecular structure, GFPs can be described as having a fluorescent signal-inherent structure with formidable chemical and biological stability that possesses the ability to be changed using biological and chemical techniques [38]. The chromophore is responsible for the GFP's fluorescence. Mostly in research, GFPs are used as a fusion tag to a protein of interest by fusing it to the terminal end of a protein gene. It can also be used as an indicator for changing conditions. However, this is restricted to certain types of GFPs or by creating new GFPs through mutation. Another common use of GFPs is to detect the proximity of two biological molecules, commonly known as FRET.

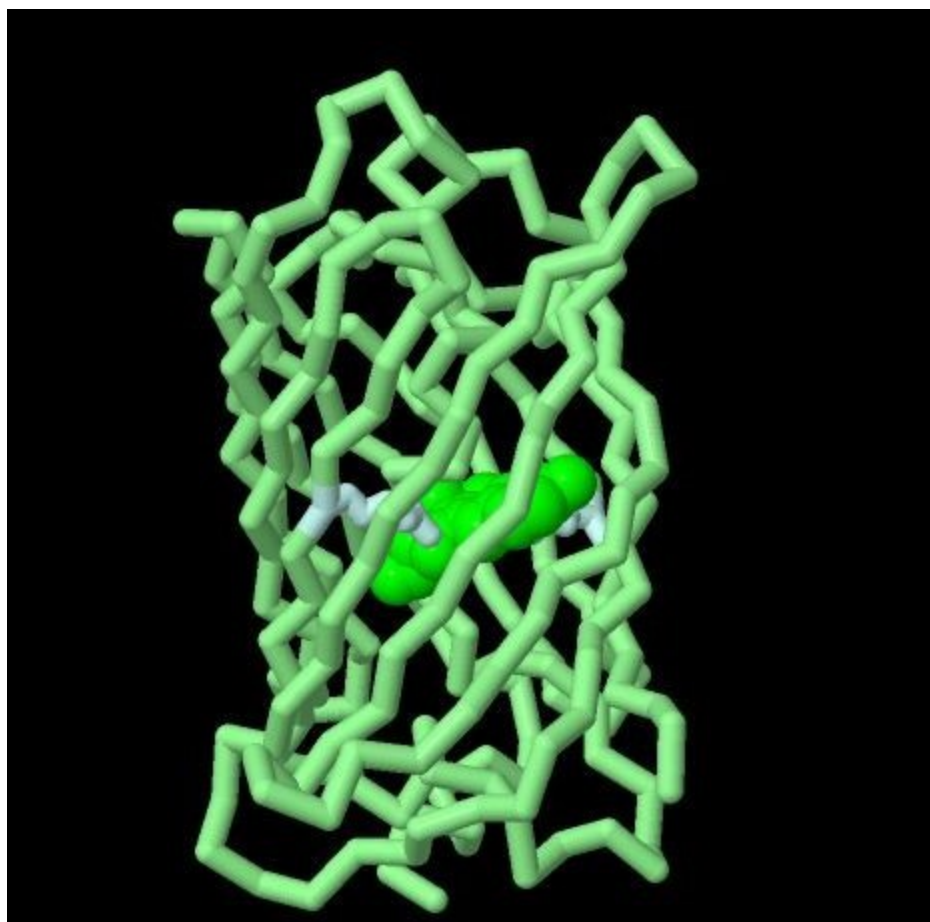


Fig. 2. Protein backbone structure of GFP (Extracted from [39]).

Experimental Basics

Fluorescence and Photobleaching

Photoluminescence describes luminescence when molecules are excited by photonic energy. Two types of photoluminescence exist: phosphorescence and fluorescence, with the latter being faster and more common. Basically, fluorescence occurs in cold bodies when they absorb light at certain wavelengths and later emit it but at a different wavelength. This is scientifically known as the emission of electromagnetic radiation in the form of light from one molecule that has been excited chemically by another source of energy. Molecular vibrations occur since there is a difference between the absorbed and emitted photons. Typically, a GFP has

an excitation peak between wavelengths of 395 nm and 475 nm. Its emission peak is somewhere around 509 nm. That of a modified GFP is 490 nm but has similar emission peak of a normal GFP. The term fluorescence first came about in 1852 when Stoke explained how organic and inorganic compounds, like quinine sulphate and fluoride crystals, are internally dispersed [40].

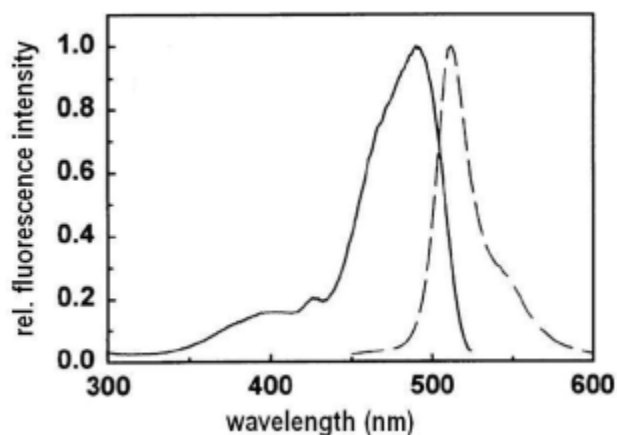


Fig. 3. GFP Spectra of an enhanced GFP (adapted from [41]).

The phenomenon of photobleaching occurs when a fluorophore permanently loses the power to fluoresce due to induced chemical damage and covalent modification. Upon transition from an excited singlet state to an excited triplet state, fluorophores tend to interact with other molecules to produce irreversible covalent modifications. The triplet state is relatively long compared to the singlet state, thus allowing excited molecules a much longer timeframe to undergo chemical reactions with components in the environment. The structure of the molecule and its environment are very influential in determining the average number of excitation and emission cycles that occur for a particular fluorophore before photobleaching. While some fluorophores are more robust and undergo thousands or millions of cycles before bleaching, others bleach quickly after emitting a few photons.

Aleksander Jablonski, through a diagram (Fig. 4), illustrated the detailed process of photobleaching. It showed specific energy level transitions that happen during molecular excitation [42].

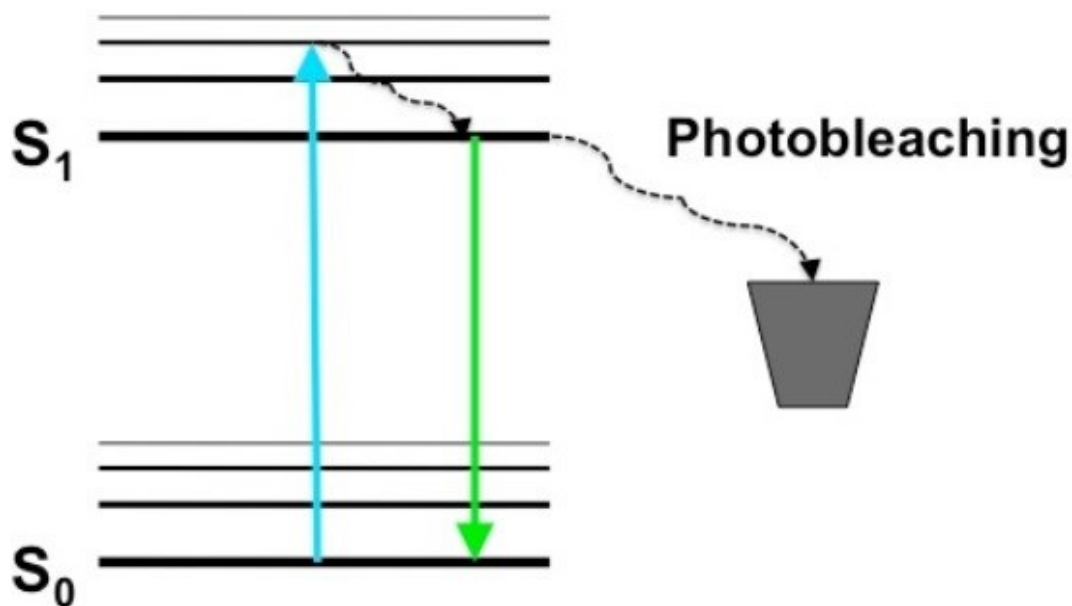


Fig. 4. A modified Jablonski Diagram. Shows what happens when a fluorophore absorbs a photon and gets excited to another energy level. The molecule then returns to the ground state after it emits the photon as fluorescence.

Absorption-Emission Cycle

Three main processes occur during fluorescence and all take place at very separate intervals. As said previously, when a fluorophore is bombarded with light, it is first excited to a higher energy level called the excited electronic state, S_1 . This happens in femtoseconds. The rapid vibrational relaxation to the lowest energy from the excited state level happens in about a picosecond or less. Fluorescence occurs during the relaxation to ground state when there are

longer wavelength photons emitted. Lifetimes for fluorescence are slower than the vibration relaxation by four orders of magnitude. Stoke, through his experiment [4], concluded that excitation light had a shorter wavelength than emitted light from the fluorescent molecules. This is called “Stokes shift,” which represents the energy lost during the excited state.

Fluorophores

Fluorophores that are used as markers must not inhibit the functions of the molecule to be investigated. Additionally, the fluorophores need to be bright and very stable under low illumination. Also, fluorophores must bleach fast and irreversibly under intense illumination during the bleaching period. This helps acquire the image before and after the bleach process. There are some photobleaching processes that are reversible, such as when the molecules remain in a dark but stable state for a long time [43]. They may reverse depending on the solute, solvent, and analytic interaction but the effect is negligible in aqueous solutions [43], [44]. Fluorophores used in early studies of photobleaching were immobile in solvents and sometimes in oxygen-deprived vacuums.

Confocal Laser Scanning Microscope (CLSM)

FRAP experiments are normally performed on commercially available CLSMs equipped with an acousto-optical tunable filter. The user may change the ROI. The intensity of the laser is controlled with an acoustic-optic tunable filter (AOTF). The AOTF allows the modulation of intensity of the laser’s illumination, which enables the user to vary the intensity pixel by pixel. The monitoring beams scan the sample with constant low laser intensity for imaging. The fluorescence intensity is then extracted from the set of pixels inside a circle. Wide field optical epi-fluorescence microscopes were the traditional equipment used in microscopy. They had a light source mostly from a mercury lamp. The image from the secondary fluorescence emission is viewed in the eyepieces or by the camera. Optical filters were used to separate the excitation

lights from the emission lights. One major advantage of the wide field optical epi-fluorescence microscopes is that excitation occurs through the whole volume instead of occurring in the plane of focus. This shrouds the resolution of features in the objectives' focal plane.

Due to the use of the laser as a source of illumination in CLSM, excitation bandwidth is determined by the source, which makes it narrower. Also CLSM can scan samples sequentially, point by point, or with multiple points at once. The pixel information is assembled into an image, which results in the acquisition of optical sections with high contrast and high resolution rather than projected through an eyepiece. Fluorescence is detected using the photomultiplier tube (PMT). The photomultipliers are used for amplifying a faint signal approximately one million times without introducing noise. One main advantage of confocal microscopy is its ability to produce blur-free images of thick specimens at various depths.

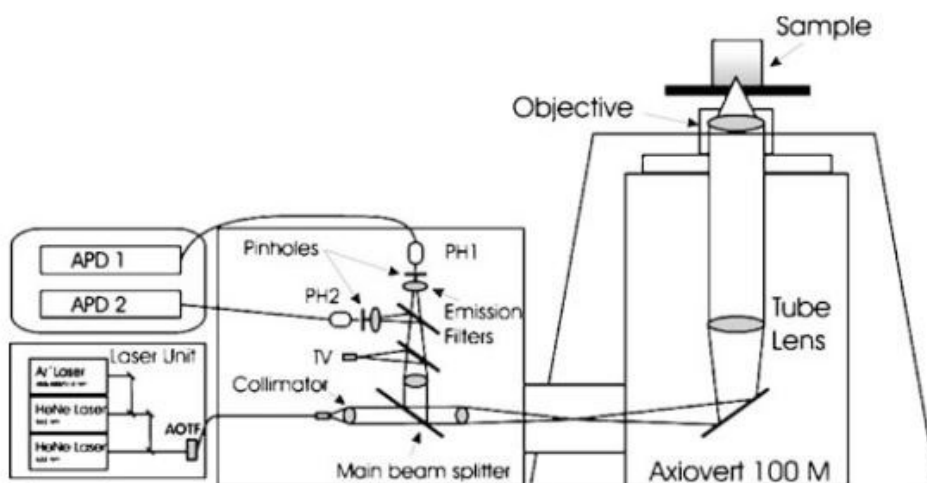


Fig. 5. Setup of a ConfoCor2 (Zeiss). Consists of an inverted confocal microscope equipped with units for scanning, three different laser sources, a fluorescence cross correlation spectroscopy and a FCS (Adapted from [45]).

The theory involved in CLSM is basically like that of a conventional optical microscope. The main difference is the use of a laser beam instead of a lamp. The laser light's intensity is

adjusted by neutral density filters. Two mirrors tilt beams in a faster fashion. CLSM uses a pair of pinhole apertures to limit the specimen's focal plane to a confined volume in size. Briefly, the CLSM works by passing a laser beam through a light source aperture. The beam is then focused by an objective lens into a small area on the surface of the sample and an image is built up pixel-by-pixel, collecting the emitted photons from the fluorophores in the sample. For molecules with an assumed high diffusion constant, more imaging speed and laser power is needed.

Breakdown of CLSM Components

The CLSM has the following parts:

- **Laser:** The laser used depends on the type of fluorophore used in the experiment and it acts as the source of light.
- **Beam splitter:** Serves as a filter for separating the excitation light from the emitted light in the fluorescence beam path.
- **Scanner:** Contains at least two mirrors that guide the focused laser beam pixel by pixel.
- **Objective lens:** Determines the optical image formation and resolution of the system. It is an important part of the microscope.
- **Z- Control:** Enables focusing on any focal plane within the sample. Motorized Z-steppers allow precise movements of at most 10 nm in the axial direction.
- **PMT:** Collects photons that are emitted by transforming light signals to electrical signals.
- **Pinhole:** Serves as the mechanical iris. It is found in the intermediate image plane. It gets rid of most of the out-of-focus light from the image, thus, providing optical

sectioning capacity. Its size can be changed by using the software on the PC and it is dependent on the properties of the objective lens.

Acousto-Optic Tunable Filter

Acousto-optic tunable filter (AOTF) is used to rapidly and dynamically select a specific wavelength from a laser source. An AOTF designed for microscopy typically consists of a tellurium dioxide or quartz anisotropic crystal to which a piezoelectric transducer is bonded. The AOTF has the capability to allow the selection of user defined areas (ROI), intensity, and/or illumination wavelength on a pixel-by-pixel basis while maintaining a high scan rate.

Qualitative FRAP

Researchers can measure the concentration and an accurate position in fluorescence microscopy with the use of a fluorescent dye as a tag. There is a rapid exchange between the nucleoplasm and other compartments in the nucleus resulting in a dynamic steady-state, causing protein concentrations to be in equilibrium. Even though an individual is able to track the steady-state compartments, he or she cannot directly reveal the movement of each protein [20], [35]. FRAP has been vital in the study of protein mobility since the development of fluorescent protein technologies and the confocal microscope.

Principles of FRAP

Basically, in FRAP experiments, fluorophores are photobleached in a specific part of a membrane with high intensity so that that part of the cell can no longer illuminate. Naturally, non-bleached areas of the cell diffuse into the bleached area. Proteins interact in vivo and that determines their mobility. This leads to recovery of fluorescence in that area under a low laser power.

FRAP occurs in the following summarized steps [1].

1. Identify the part of the region which will be bleached (ROI).
2. Acquire control images in order to measure the pre-bleach laser intensity.
3. Images should be taking without delay after short but high laser intensity bombardment in ROI.
4. Record the recovery process in the area.
5. Changes in intensity in that area show the sum of movements of the fluorophores.

Fluorophores Used in FRAP

There are many fluorophores that can be used in FRAP experiments. However, if these fluorophores are used as markers they should not have some property of the molecule to be investigated. As aforementioned, they should be photo stable. That is, they should be bright and stable under low intensity illumination during image acquisition. Also, during high intensity illumination they should bleach fast and irreversibly.

Quantitative FRAP

This section deals with the data gained from a FRAP experiment. A FRAP experiment is time-dependent. The FRAP recovery curve shows the time it takes for the recovery of fluorescence intensity at a bleached spot.

Normalizing FRAP Data

To enable researchers to accurately measure results, the data need to be normalized [11]. This needs to be done since we have to take into consideration the changes in the total fluorescence intensity during the whole experiment. In the process of photobleaching, researchers make some fluorescent proteins non-fluorescent, even though they are not supposed to be. Thus, reducing the theoretical maximum intensity, the bleached area can recuperate to its pre-bleached intensity after photobleaching. Also, through this process of collecting data for the

recovery curve, the cells are exposed to laser illumination, sometimes causing them to be photobleached too. About 10% of fluorescence is lost during the bleaching process and 5% is lost in the imaging process. A normalization method introduced by Phair and Misteli is used in FRAP experiments [46]. They normalized the fluorescence signal in the ROI to change the total fluorescence as follows:

$$F(t) = \frac{F_{raw}(t) - F_0}{F_i - F_0}$$

where $F_{raw}(t)$ is intensity in the ROI, F_0 is intensity in ROI during bleach and F_i is pre-bleach intensity.

Laser Profile

The scanning laser profiles used in photobleaching are approximated using a Gaussian function [15], [27], [28], [47], [48]. This is given as:

$$I_r(x) = I_0 \prod_{j=1}^N \frac{1}{g_j} \exp\left(-\frac{2x_j^2}{r_j^2}\right)$$

where N is the spatial dimension, $x = (x_1, x_2, \dots, x_N)$ and $r = (r_1, r_2, \dots, r_N)$ representing the nominal radius defined as half the width at e^{-2} height of the maximal laser intensity profile.

The maximal laser intensity profile is $I_0/\overline{g_j}$ for $j = 1, 2, 3, \dots, N$.

Biophysical Properties

The diffusion coefficient and mobile fraction of a fluorescent molecule can be determined from our experiments. The latter is just a fraction of fluorescent proteins that can diffuse into the bleached area during the experimental process [49]. This is derived by

$$R = \frac{F_\infty - F_0}{F_I - F_0}$$

where F_{∞} is the fluorescence in the bleached area after full recovery, F_t is the fluorescence before bleaching, and F_0 is the fluorescence just after bleaching.

The former, termed diffusion coefficient, D , is the mobility in proteins due to diffusion and can be calculated using the diffusion time $\tau_{1/2}$. $\tau_{1/2}$ is known as the characteristic diffusion time; this is the time necessary for fluorescence to half recover between the fluorescence level after F_0 and F_{∞} . Using a model by Axelrod et al. [15], for two-dimensional diffusion and circular bleached spots by a Gaussian laser beam, it can be derived as:

$$D = \frac{\omega^2}{4\tau_{1/2}}$$

where ω is half the width of the laser beam intensity at a height of $\exp(-2)$.

MATHEMATICAL MODEL

Diffusion Modelling

Even though it is easy to conduct a FRAP experiment on a CLSM, the difficult part is analyzing the experiment for biophysical parameters. There are several ways of interpreting protein dynamics: recovery curve and characteristic diffusion time. However, it is impossible to get these parameters due to the shape of the recovery curves. The most definite way of getting quantitative results is to make numerical simulations of solving spatiotemporal models taking real life geometry of the cell into account. This thesis examines this concept further. Researchers can use diffusion and cell reactions (binding and unbinding) to describe protein dynamics. Researchers, first of all, need to understand in vivo protein dynamics to explain what the FRAP curves mean. In these analyses, we will have to make the assumption that solutions of reaction-diffusion systems are nontrivial. A better method for deriving the diffusion coefficient, binding,

and dissociation constants is to simulate a mathematical reaction-diffusion model by parameter estimation [24].

In biology, active transport is the net movement of molecules in and out of the cell across the cell membrane along a concentration gradient due to Brownian motion. Diffusion can be modeled spatiotemporally by either using the stochastic model or finding it deterministically. The stochastic model involves random walk, whilst the deterministic approach involves the use of the diffusion law by Adolf Fick. The former is better in this case since the concentration gradient can be shown through diffusion population. After photobleaching, there are two kinds of proteins in the experiment: bleached proteins and fluoresced proteins. Therefore the combination of these two proteins creates a concentration gradient. In deriving the diffusion coefficient, the diffusion equation in one dimension is given by:

$$\frac{dC(x, t)}{dt} = D \frac{d^2C}{dx^2}$$

where C is the concentration. In the three-dimensional approach, the flux of mass can be calculated with the formula below

$$\frac{dC}{dt} = -\nabla \vec{J} = D \left(\frac{d^2C}{dx^2} + \frac{d^2C}{dY^2} + \frac{d^2C}{dZ^2} \right) = D \nabla^2 C$$

where \vec{J} is the flux. It describes the time dependence of the diffusion of a substance with regards to Fick's 2nd law.

Diffusion Coefficient

The diffusion constant, D , is a proportionality factor describing the mass of the substance that diffuses through a unit surface, in a unit time, and at a concentration gradient of unity. Simply put, it is the rate an object diffuses in fluid. It is dependent on the molecule's size, temperature, and pressure. D is derived from the Stokes-Einstein Equation [50] as:

$$D = \frac{k_B T}{6\pi\eta r}$$

where k is the Boltzmann constant, T is the absolute temperature, η is the dynamic viscosity, and r is the radius of the spherical particle.

Boundary Conditions

Boundary conditions are information describing how the molecules are connected to each other, to the larger cellular context, and to external constraints. Boundary conditions describe where the edges of the molecules are and how they adapt. When we talk of a boundary, it can be related to dimensionality, that is, the degree of freedom a component has in the system to move. Whilst initial conditions are obtained from the photobleaching process, boundary conditions are assumed from biological considerations. A nuclear membrane serves as a barrier of diffusion in the cell between the cytoplasm and the nucleus. We can use parabolic partial differential equations to show protein dynamics by showing that there is little to no flux through the nuclear membrane mathematically. Using the no-flux Neumann boundary conditions G , the boundary equation is given as:

$$\vec{n}\nabla f|_{\Gamma} = 0$$

$\vec{n}\nabla f$ represents the normalized derivative of the concentration at the boundaries. Typical of most FRAP experiments, the bleached region is chosen to be infinite to allow the molecules to evenly distribute across the boundary. However, this condition does not happen in real life. There is a need to determine the impact of this condition on the model by using other boundary conditions.

Dirichlet Boundary Conditions

This boundary specifies the value of the function on a particular surface $T = f(r, t)$, which helps find values that a solution needs to take on along the boundary of the domain when imposed on a differential equation. An interpretation of these boundary conditions for the one-

dimensional heat equation can provide a better explanation to this boundary condition. Setting a Dirichlet boundary condition means imposing the value for the temperature in one edge of the one-dimensional domain (e.g. a metal bar); that is, fixing the value for the temperature for the solution at that edge.

Neumann Boundary Conditions

Neumann boundary gives the normal derivative of the function on the surface $\partial T / \partial n = \hat{n} \cdot \nabla T = f(r, t)$. Setting a Neumann boundary condition means to impose the flux of heat through that edge. If the Neumann boundary condition is set to zero, that is, a homogeneous boundary condition, it means that the edge of the bar is isolated, and no flux of heat enters the bar.

Recovery Curve

As discussed earlier in the chapter, the solutions can be derived analytically or using the numeric approach. It provides the time-dependent values of the concentrations. However the fluorescence intensity cannot be obtained this way. The recovery curve can only be obtained from the FRAP experiment itself. Both results are compared: the simulated model and that of the real experiment. Once this is done, the fluorescence intensity image is created by transforming the fluorophore distribution [18].

In this modern era, FRAP experiments occur on confocal laser scanning microscopes where images are formed mathematically by convolution. Using this, the fluorescence intensity recovery can easily be extracted from the generated image, especially if all experimental assumptions and conditions [18] are met. It seems the laser beam is stationary and has a uniform intensity distribution; objectives of low numerical apertures are used and radial resolution of the detecting laser beam is smaller than that of the scanned structure.

Numerical Solution

Researchers can only be able to determine factors that influence FRAP experiments by using simulations, experiments, or other scientific methods to determine quantitatively the impact of the various factors. Through the use of partial differential equations (PDEs), the FRAP data can be mathematically described. PDEs take into account the following:

1. Spatio-temporal process: This is the most important factor since it deals with movement and interactions in the cell: diffusion and reaction.
2. Initial conditions: at time $t = 0$; the behavior and characteristics of the modeled system are checked at that point. There may be different types of such approximation but for FRAP simulations, bleaching has to be approximated immediately after observance of fluorescence distribution.
3. Boundary conditions: This shows the behavior of the system at the boundaries of the geometry.
4. Geometry of a domain: The space in which the experiments will be performed must be feasible. Researchers can either assume and simplify these geometries or go ahead with the real cell geometries.

Analytic Solution

The fluorescence recovery within the bleach spot can be derived by making the assumption that the bleach spot must have a size relatively smaller than that of the fluorescent compartment. The nucleus is assumed to have an infinite size. Due to the infinite size of the nucleus, the condition at the boundaries is $C(r \pm \infty, t) = C_{eq}$ for all t . Fluorescence intensity also recovers to the initial pre-bleach values making some small amount of fluorescence lost.

The geometry of the composite cylindrical regions can be determined due to the infinite nucleus assumption and the circular bleaching spot. The binding state model can be solved using the analogy in [51].

Chapter 3

METHODOLOGY & ANALYSIS

This study is a quantitative study even though it also includes experimental design. This chapter includes the research methods used and numerical techniques applied in solving the equations. It involves all derivations for the FRAP models previously listed in this paper. Before researchers can use these FRAP models, they need to perform the experiment in real life and collect all necessary data.

Summary of Steps to Perform Experiment

Below are the steps involved in completing the experiment :

1. First of all, the user needs to find a cell region to be bleached, that is, the ROI.
2. Acquire control images to measure intensity before bleaching process.
3. Perform confocal FRAP using a bleach spot with an arbitrary radius but within the ROI.
4. Analyze the first post-bleach image.
5. Run analysis depending on the type of radius and post-bleach profile: exponential or Gaussian.

Assuming the fluorescence intensity is linearly proportional to the concentration of fluorophores ($F \propto C$), the fluorescence intensity (F) in an ROI is given as:

$$F(t) = q \int_{\Omega} [\epsilon I_r(x)] C(x, t) dx \quad (3.1)$$

where Ω is the domain of diffusion and q is the quantum yields mostly known as the proportionality constant. Fluorescence concentration about the space x and at time t is represented by $C(x, t)$. This is obtained by recording the concentration under low laser intensity

after an irreversible photobleaching of the region of interest. Kinetics of fluorophores affect how FRAP curves may look. To find the diffusion constants, the FRAP curves are fit to the diffusion equation. The scanning laser profile for photobleaching as a Gaussian approximation is found as

$$I_r(x) = I_0 \prod_{j=1}^N \frac{1}{g_j} \exp\left(-\frac{2x_j^2}{r_j^2}\right) \quad (3.2)$$

where $r = (r_1, r_2, \dots, r_N)$ is defined as the nominal radius defined as the half width at e^{-2} of the height of the maximal laser intensity profile $(I_0/\overline{g_j})$ for $j = 1, 2, \dots, N$ where N is the spatial dimension and $x = (x_1, x_2, \dots, x_N)$. $\overline{g_j} = \int_{\Omega} \exp\left(-\frac{2x_j^2}{r_j^2}\right) dx$

Using Neumann or Dirichlet conditions, $C(x,t)$ can be found by solving

$$C_t = D\Delta C \quad (3.3)$$

where $\Delta = \sum_{j=1}^N \frac{\partial^2}{\partial x_j^2}$ and $D(\mu m^2/s)$ is a diffusion coefficient.

It is assumed that there is 100% recovery of fluorescence in infinite domain in a pre-bleach steady state. Post bleaching fluorescence intensity is an exponential function if bleaching is followed by a first-order kinetics of photobleaching. It has been empirically tested that the post-bleach fluorophore concentration profile for a ROI with radius r_j 's (nominal radii) is

$$C(x, 0) = C_i \left[1 - K \prod_{j=1}^N \exp\left(-\frac{2x_j^2}{\omega_j^2}\right) \right] \quad (3.4)$$

where C_i is the fluorescence molecule concentration at a prebleach steady state, K is the depth of the bleaching parameter, found using the initial postbleach fluorescence intensity of FRAP data, and ω_j is the effective radii. However, mostly, the effective radii are greater than the nominal radii due to diffusion during scans.

There is also an assumption that fluorophore concentration and fluorescence intensity are normalized to the prebleach steady state fluorescence intensity (F_i) and the prebleach steady state fluorophore concentration (C_i) respectively:

$$\begin{cases} C_i = 1 \\ F_i = q\epsilon I_0 C_i = 1 \end{cases} \quad (3.5)$$

where q is the quantum yield, I_0 is the total laser intensity, and ϵ is the attenuation factor.

Mathematical Derivation

FRAP Models for Pure Diffusion in 1D (\mathbb{R})

Consider a 1D diffusion equation with diffusion coefficient D , given an initial condition and the Gaussian laser profile:

$$C_t = DC_{xx} \quad (3.6)$$

$$C(x, 0) = C_i \left[1 - K \prod_{j=1}^N \exp\left(-\frac{2x_j^2}{\omega_j^2}\right) \right] = 1 - Kg_\omega(y) \quad (3.7)$$

$$I_r(x) = I_0 G_r(x)$$

This is a normal distribution with $G_r(x) = (2/\pi)^{1/2}/r \cdot \exp(-\frac{2x^2}{r^2}) = \frac{1}{\frac{r}{2}\sqrt{2\pi}} \exp\left(-\frac{x^2}{2\left[\frac{r}{2}\right]^2}\right)$ having

a standard deviation $r/2$. Notice that

$$\begin{aligned} \int I_r(x) dx &= \int I_0 G_r(x) dx \\ &= I_0 \int \frac{1}{\frac{r}{2}\sqrt{2\pi}} \exp\left(-\frac{x^2}{2\left[\frac{r}{2}\right]^2}\right) dx \\ &= I_0 \end{aligned}$$

If $g_r(x) = \exp(-2x^2/r^2)$, then

$$G_r(x) = \frac{\sqrt{2/\pi}}{r} \exp\left(-\frac{2x^2}{r^2}\right) = \frac{g_r(x)}{\bar{g}} \quad (3.8)$$

where $\bar{g} = \int g_r(x) dx = \frac{r}{\sqrt{2/\pi}}$.

For the case of a Gaussian type detection laser profile, the FRAP formula in \mathbb{R} is given by

$$\begin{aligned} F(t) &= q \int_{\mathbb{R}} [\epsilon I_r(x)] C(x, t) dx \\ &= q \int_{\mathbb{R}} [\epsilon I_0 G_r(x)] \Phi(y, t) * C(x, 0) dx \\ &= q \epsilon I_0 C_i \int_{\mathbb{R}} \left(\frac{g_r(x)}{\bar{g}} \right) \int_{\mathbb{R}} (1 - K g_\omega(y)) \frac{\exp\left(-\frac{|x-y|^2}{4Dt}\right)}{\sqrt{4\pi Dt}} dy dx \\ &= F_i \int_{\mathbb{R}} \int_{\mathbb{R}} \left(\frac{g_r(x)}{\bar{g}} \right) \frac{\exp\left(-\frac{|x-y|^2}{4Dt}\right)}{\sqrt{4\pi Dt}} dy dx \\ &\quad - F_i \int_{\mathbb{R}} \int_{\mathbb{R}} \left(\frac{g_r(x)}{\bar{g}} \right) (K g_\omega(y)) \frac{\exp\left(-\frac{|x-y|^2}{4Dt}\right)}{\sqrt{4\pi Dt}} dy dx \\ &= F_i - F_i \int_{\mathbb{R}} \int_{\mathbb{R}} \left(\frac{g_r(x)}{\bar{g}} \right) (K g_\omega(y)) \frac{\exp\left(-\frac{|x-y|^2}{4Dt}\right)}{\sqrt{4\pi Dt}} dy dx \end{aligned}$$

where F_i is the prebleach fluorescence intensity due to prebleach steady state fluorescence molecule concentration, C_i . Note that:

$$\begin{aligned} &\int_{\mathbb{R}} g_r(x) g_\omega(x + \theta\eta) dx \\ &= \int_{\mathbb{R}} \exp\left(-\frac{2x^2}{r^2} - \frac{2(x + \theta\eta)^2}{\omega^2}\right) dx \end{aligned}$$

$$\begin{aligned}
&= \int_{\mathbb{R}} \exp\left(-\frac{2x^2\omega^2 + 2r^2(x + \theta\eta)^2}{r^2\omega^2}\right) dx \\
&= \int_{\mathbb{R}} \exp\left(-\frac{2(\omega^2 + r^2)x^2 + 4r^2\theta\eta x + 2r^2(\theta\eta)^2}{r^2\omega^2}\right) dx \\
&= \int_{\mathbb{R}} \exp\left(-\frac{2(\omega^2 + r^2)}{r^2\omega^2}\left(x + \frac{r^2\theta\eta}{r^2 + \omega^2}\right)^2\right) \exp\left(-\frac{2\theta^2\eta^2}{(r^2 + \omega^2)}\right) dx
\end{aligned}$$

By letting $a = \frac{\sqrt{2(\omega^2 + r^2)}}{r\omega}$ and $b = \sqrt{\frac{2\theta^2}{r^2 + \omega^2}}$

$$\begin{aligned}
&\int_{\mathbb{R}} g_r(x) g_\omega(x + \theta\eta) dx \\
&= \int \exp(-b^2\eta^2) \exp\left(-a^2\left(x + \frac{r^2}{r^2 + \omega^2}\theta\eta\right)^2\right) dx \\
&= \int \exp(-b^2\eta^2) \int \exp(-a^2x^2) dx \\
&= \exp(-b^2\eta^2) \int \exp(-a^2x^2) dx \\
&= \frac{\sqrt{\pi}}{a} \exp(-b^2\eta^2) \\
&= \frac{r\omega\pi}{2(r^2 + \omega^2)} \exp\left(-\frac{2\theta^2\eta^2}{r^2 + \omega^2}\right).
\end{aligned}$$

If $y = x + \sqrt{4Dt} \eta$ ($dy = \sqrt{4Dt} d\eta$), then $y - x = \sqrt{4Dt} \eta$

$$\begin{aligned}
F(t) &= F_i - F_i \int_{\mathbb{R}} \int_{\mathbb{R}} \left(\frac{g_r(x)}{\bar{g}}\right) (K g_\omega(x + \sqrt{4Dt} \eta)) \frac{\exp\left(-\frac{|x - y|^2}{4Dt}\right)}{\sqrt{4\pi Dt}} \sqrt{4Dt} d\eta dx \\
&= F_i - F_i \int_{\mathbb{R}} \int_{\mathbb{R}} \left(\frac{g_r(x)}{\bar{g}}\right) (K g_\omega(x + \sqrt{4Dt} \eta)) \exp(-\eta^2) d\eta dx \\
&= F_i - F_i \frac{K\sqrt{2/\pi}}{r\sqrt{\pi}} \int_{\mathbb{R}} \left(\int_{\mathbb{R}} g_r(x) (g_\omega(x + \sqrt{4Dt} \eta)) dx\right) \exp(-\eta^2) d\eta
\end{aligned}$$

$$\begin{aligned}
&= F_i - F_i \frac{K\sqrt{2/\pi}}{r\sqrt{\pi}} \int_{\mathbb{R}} \left(\frac{r\omega\pi}{\sqrt{2(r^2 + \omega^2)}} \exp\left(-\frac{2\theta^2\eta^2}{r^2 + \omega^2}\right) \right) \exp(-\eta^2) d\eta \\
&= F_i - F_i \frac{K\omega}{\sqrt{(r^2 + \omega^2)}} \int_{\mathbb{R}} \exp\left(-\frac{(2\theta^2 + \omega^2 + r^2)}{r^2 + \omega^2} \eta^2\right) \\
&= F_i - F_i \frac{K\omega\sqrt{2}}{\sqrt{2(2\theta^2 + \omega^2 + r^2)}} \\
&= F_i - F_i \frac{K}{\sqrt{\left(1 + \left(\frac{r}{\omega}\right)^2 + 2\frac{t}{\tau_D}\right)}} \tag{3.9}
\end{aligned}$$

where $\tau_D = \frac{\omega^2}{4D}$.

FRAP Models for Pure Diffusion in 2D (\mathbb{R}^2)

For the case of a Gaussian-type detection laser profile, the FRAP formula in \mathbb{R}^2 is given by:

$$\begin{aligned}
F(t) &= q \int_{\mathbb{R}^2} [\epsilon I_r(x)] C(x, t) dx \\
&= q \int_{\mathbb{R}^2} [\epsilon I_0 G_r(x)] \Phi(y, t) * C(x, 0) dx \\
&= q \epsilon I_0 C_i \int_{\mathbb{R}^2} \left(\frac{g_r(x)}{\bar{g}} \right) \int_{\mathbb{R}^2} (1 - K g_\omega(y)) \frac{\exp\left(-\frac{|x-y|^2}{4Dt}\right)}{4\pi Dt} dy dx \\
&= F_i \int_{\mathbb{R}^2} \int_{\mathbb{R}^2} \left(\frac{g_r(x)}{\bar{g}} \right) (1 - K g_\omega(y)) \frac{\exp\left(-\frac{|x-y|^2}{4Dt}\right)}{4\pi Dt} dy dx
\end{aligned}$$

$$\begin{aligned}
&= F_i \int_{\mathbb{R}^2} \int_{\mathbb{R}^2} \left(\frac{g_r(x)}{\bar{g}} \right) \frac{\exp\left(-\frac{|x-y|^2}{4Dt}\right)}{4\pi Dt} dy dx \\
&\quad - F_i \int_{\mathbb{R}^2} \int_{\mathbb{R}^2} \left(\frac{g_r(x)}{\bar{g}} \right) K g_\omega(y) \frac{\exp\left(-\frac{|x-y|^2}{4Dt}\right)}{4\pi Dt} dy dx \\
&= F_i - F_i \int_{\mathbb{R}^2} \int_{\mathbb{R}^2} \left(\frac{g_r(x)}{\bar{g}} \right) (K g_\omega(y)) \frac{\exp\left(-\frac{|x-y|^2}{4Dt}\right)}{4\pi Dt} dy dx
\end{aligned}$$

where F_i is the prebleach fluorescence intensity due to prebleach steady state fluorescence molecule concentration, C_i .

Let $y = x + \sqrt{4Dt} \eta$ ($dy = (\sqrt{4Dt})^2 d\eta$, i.e

$$\begin{cases} y_1 = x_1 + \sqrt{4Dt} \eta_1 \\ y_2 = x_2 + \sqrt{4Dt} \eta_2 \end{cases} \quad (3.10)$$

and

$$\begin{cases} dy_1 = \sqrt{4Dt} d\eta_1 \\ dy_2 = \sqrt{4Dt} d\eta_2 \end{cases} \Rightarrow dy = dy_1 dy_2 = 4Dt \eta_1 \eta_2.$$

Then $y - x = \sqrt{4Dt} \eta$, and

$$\begin{aligned}
F(t) &= F_i - F_i \int_{\mathbb{R}^2} \int_{\mathbb{R}^2} \left(\frac{g_r(x)}{\bar{g}} \right) (K g_\omega(x + \sqrt{4Dt}\eta)) \frac{\exp\left(-\frac{4Dt|\eta|^2}{4Dt}\right)}{4\pi Dt} (4Dt) d\eta dx \\
&= F_i - F_i \int_{\mathbb{R}^2} \int_{\mathbb{R}^2} \left(\frac{g_r(x)}{\bar{g}} \right) (K g_\omega(x + \sqrt{4Dt}\eta)) \exp\left(-\frac{4Dt|\eta|^2}{4Dt}\right) d\eta dx \\
&= F_i - F_i \int_{\mathbb{R}^2} \int_{\mathbb{R}^2} \left(\frac{g_r(x)}{\bar{g}} \right) (K g_\omega(x + \sqrt{4Dt}\eta)) \exp(-|\eta|^2) d\eta dx \\
&= F_i - F_i \frac{2K}{r^2 \pi^2} \int_{\mathbb{R}^2} \int_{\mathbb{R}^2} \left((g_r(x)) g_\omega(x + \sqrt{4Dt}\eta) \right) \exp(-|\eta|^2) d\eta
\end{aligned}$$

Now, denote $\theta = \sqrt{4Dt}$ and note that,

$$\begin{aligned}
g_r(x) &= \exp\left(-\frac{2|x|^2}{r^2}\right) \\
&= \exp\left(-\frac{2(x_1^2 + x_2^2)}{r^2}\right) \\
&= \exp\left(-\frac{2x_1^2}{r^2}\right) \exp\left(-\frac{2x_2^2}{r^2}\right) \\
&= g_r(x_1)g_r(x_2)
\end{aligned}$$

and

$$\begin{aligned}
g_\omega(x + \theta\eta) &= \exp\left(-\frac{2|x + \theta\eta|^2}{\omega^2}\right) \\
&= \exp\left(-\frac{2((x_1 + \theta\eta_1)^2 + (x_2 + \theta\eta_2)^2)}{\omega^2}\right) \\
&= g_\omega(x_1 + \theta\eta_1)g_\omega(x_2 + \theta\eta_2).
\end{aligned}$$

Hence,

$$\begin{aligned}
\int_{\mathbb{R}^2} g_r(x) g_\omega(x + \theta\eta) dx &= \int_{\mathbb{R}^2} g_r(x_1)g_r(x_2)g_\omega(x_1 + \theta\eta_1)g_\omega(x_2 + \theta\eta_2) dx_1 dx_2 \\
&= \int g_r(x_1)g_\omega(x_1 + \theta\eta_1) dx_1 \int g_r(x_2)g_\omega(x_2 + \theta\eta_2) dx_2 \\
&= \int \exp\left(-\frac{2x_1^2}{r^2}\right) \exp\left(-\frac{2(x_1 + \theta\eta_1)^2}{\omega^2}\right) dx_1 \int \exp\left(-\frac{2x_2^2}{r^2}\right) \exp\left(-\frac{2(x_2 + \theta\eta_2)^2}{\omega^2}\right) dx_2 \\
&= \frac{\sqrt{\pi}}{a} \exp(-b^2\eta_1^2) \frac{\sqrt{\pi}}{a} \exp(-b^2\eta_2^2)
\end{aligned}$$

where $b = \sqrt{\frac{2\theta^2}{\omega^2 + r^2}}$ and $a = \frac{\sqrt{2(\omega^2 + r^2)}}{r\omega}$. Therefore,

$$F(t) = F_i - F_i \frac{2K}{r^2 \pi^2} \int_{\mathbb{R}^2} \int_{\mathbb{R}^2} (g_r(x)g_\omega(x + \theta\eta) dx) \exp(-|\eta|^2) d\eta$$

$$\begin{aligned}
&= F_i - F_i \frac{2K}{r^2 \pi^2} \int_{\mathbb{R}^2} \left(\frac{\sqrt{\pi}}{a} \exp(-b^2 \eta_1^2) \frac{\sqrt{\pi}}{a} \exp(-b^2 \eta_2^2) \right) \exp(-|\eta|^2) d\eta \\
&= F_i - F_i \frac{2K}{a^2 r^2 \pi} \int_{\mathbb{R}^2} (\exp(-b^2 + 1)(\eta_1^2 + \eta_2^2)) d\eta_1 d\eta_2 \\
&= F_i - F_i \frac{2K}{a^2 r^2 \pi} \frac{\sqrt{\pi}}{\sqrt{b^2 + 1}} \frac{\sqrt{\pi}}{\sqrt{b^2 + 1}} \\
&= F_i \left(1 - \frac{K}{1 + \left(\frac{r}{\omega}\right)^2 + 2 \frac{t}{\tau_D}} \right). \tag{3.11}
\end{aligned}$$

FRAP Models for Pure Diffusion in nD (\mathbb{R}^N)

Using the similar steps as those used for FRAP models in \mathbb{R}^1 and \mathbb{R}^2 , the FRAP model for \mathbb{R}^N can be derived. The Gaussian laser profile in \mathbb{R}^N is described as

$$I_r(x) = I_0 \mathcal{G}_r(x).$$

This is a normal distribution with $\mathcal{G}_r(x_i) = \frac{\sqrt{2/\pi}}{r_i} \exp\left(-\frac{2x_i^2}{r_i^2}\right) = \frac{1}{\frac{r_i}{2}\sqrt{2\pi}} \exp\left(-\frac{x_i^2}{2\left[\frac{r_i}{2}\right]^2}\right)$ having a

standard deviation $\frac{r_i}{2}$. Define $g_{ri}(x_i) = \exp\left(-\frac{2x_i^2}{r_i^2}\right)$. In \mathbb{R}^N , for $r = (r_1, r_2, r_2, \dots, r_N)$,

$$\begin{aligned}
\mathcal{G}_r(x) &= \prod_{i=1}^N \frac{\sqrt{2/\pi}}{r_i} \exp\left(-\frac{2x_i^2}{r_i^2}\right) \\
&= \prod_{i=1}^N \frac{g_{ri}(x_i)}{\bar{g}_i} \tag{3.12}
\end{aligned}$$

where $g_r(x) = \prod_{i=1}^N g_{ri}(x_i) = \exp\left(-\sum_{i=1}^N \frac{2x_i^2}{r_i^2}\right)$ and $\bar{g} = \prod_{i=1}^N \bar{g}_i$.

For the case of a Gaussian-type detection laser profile, the FRAP in \mathbb{R}^N is given by

$$\begin{aligned}
F(t) &= q \int_{\mathbb{R}^N} [\epsilon I_0 \mathcal{G}_r(x)] C(x, t) dx \\
&= q \int_{\mathbb{R}^N} [\epsilon I_0 \mathcal{G}_r(x)] \Phi(y, t) * C(x, 0) dx \\
&= q \epsilon I_0 C_i \int_{\mathbb{R}^N} \left(\frac{g_r(x)}{\bar{g}} \right) \int_{\mathbb{R}^N} (1 - K g_\omega(y)) \frac{\exp\left(-\frac{|x-y|^2}{4Dt}\right)}{(4\pi Dt)^{N/2}} dy dx \\
&= F_i \int_{\mathbb{R}^N} \int_{\mathbb{R}^N} \left(\frac{g_r(x)}{\bar{g}} \right) (1 - K g_\omega(y)) \frac{\exp\left(-\frac{|x-y|^2}{4Dt}\right)}{(4\pi Dt)^{N/2}} dy dx \\
&= F_i \int_{\mathbb{R}^N} \int_{\mathbb{R}^N} \left(\frac{g_r(x)}{\bar{g}} \right) \frac{\exp\left(-\frac{|x-y|^2}{4Dt}\right)}{(4\pi Dt)^{N/2}} dy dx \\
&\quad - F_i \int_{\mathbb{R}^N} \int_{\mathbb{R}^N} \left(\frac{g_r(x)}{\bar{g}} \right) K g_\omega(y) \frac{\exp\left(-\frac{|x-y|^2}{4Dt}\right)}{(4\pi Dt)^{N/2}} dy dx \\
&= F_i - F_i \int_{\mathbb{R}^N} \int_{\mathbb{R}^N} \left(\frac{g_r(x)}{\bar{g}} \right) K g_\omega(y) \frac{\exp\left(-\frac{|x-y|^2}{4Dt}\right)}{(4\pi Dt)^{N/2}} dy dx
\end{aligned}$$

where F_i is the prebleach fluorescence intensity due to prebleach steady state fluorescence

molecule concentration, C_i . If $y = x + \sqrt{4Dt}\eta$ ($dy = (\sqrt{4Dt})^N d\eta$):

$$\begin{aligned}
F(t) &= F_i - F_i \int_{\mathbb{R}^N} \int_{\mathbb{R}^N} \left(\frac{g_r(x)}{\bar{g}} \right) K g_\omega(x + \sqrt{4Dt}\eta) \frac{\exp\left(-\frac{|\eta|^2}{4Dt}\right)}{(4\pi Dt)^{N/2}} (\sqrt{4Dt})^N d\eta dx \\
&= F_i - F_i \int_{\mathbb{R}^N} \int_{\mathbb{R}^N} \left(\frac{g_r(x)}{\bar{g}} \right) K g_\omega(x + \sqrt{4Dt}\eta) \exp\left(-\frac{|\eta|^2}{4Dt}\right) d\eta dx
\end{aligned}$$

$$\begin{aligned}
&= F_i - KF_i \left(\prod_{i=1}^N \frac{\sqrt{2/\pi}}{r_i} \right) \int_{\mathbb{R}^N} \left(\int_{\mathbb{R}^N} (g_r(x)) K g_\omega(x \right. \\
&\quad \left. + \sqrt{4Dt}\eta) dx \right) \exp(-|\eta|^2) d\eta.
\end{aligned}$$

Now, denote $\theta = \sqrt{4Dt}$ and note that,

$$\begin{aligned}
\int_{\mathbb{R}^N} g_r(x) g_\omega(x + \theta\eta) dx &= \int_{\mathbb{R}^N} \prod_{i=1}^N g_{r_i}(x_i) \prod_{i=1}^N g_{\omega_i}(x_i + \theta\eta_i) dx \\
&= \prod_{i=1}^N \frac{\sqrt{\pi}}{a_i} \exp(-b_i^2 \eta_i^2)
\end{aligned}$$

where $b = \sqrt{\frac{2\theta^2}{\omega_i^2 + r_i^2}}$ and $a = \frac{\sqrt{2(\omega_i^2 + r_i^2)}}{r\omega_i}$. Therefore,

$$\begin{aligned}
F(t) &= F_i - KF_i \left(\prod_{i=1}^N \frac{\sqrt{2/\pi}}{r_i} \right) \int_{\mathbb{R}^N} \left(\prod_{i=1}^N \frac{\sqrt{\pi}}{a_i} \exp(-b_i^2 \eta_i^2) \right) \left(\prod_{i=1}^N \exp(-\eta_i^2) \right) d\eta \\
&= F_i - KF_i \left(\prod_{i=1}^N \frac{\sqrt{2/\pi}}{r_i} \right) \int \frac{\sqrt{\pi}}{a_i} \exp(-b_i^2 + 1) \eta_i^2 d\eta_i \\
&= F_i - KF_i \prod_{i=1}^N \frac{\sqrt{2}}{a_i r_i} \left(\frac{\sqrt{\pi}}{\sqrt{b_i^2 + 1}} \right) \\
&= F_i - KF_i \prod_{i=1}^N \left(\frac{\sqrt{2}}{\frac{\sqrt{2(\omega_i^2 + r_i^2)}}{r_i \omega_i} r_i \sqrt{\frac{2\theta^2}{\omega_i^2 + r_i^2} + 1}} \right) \\
&= F_i - KF_i \prod_{i=1}^N \left(\frac{\omega_i \sqrt{\pi}}{\sqrt{8(Dt)^2 + \omega_i^2 + r_i^2}} \right)
\end{aligned}$$

$$= F_i - KF_i \prod_{i=1}^N \left(\frac{\omega_i \sqrt{\pi}}{\sqrt{8(Dt)^2 + \omega_i^2 + r_i^2}} \right) \quad (3.13)$$

$$F(t) = F_i - KF_i \prod_{i=1}^N \left(\frac{K}{\sqrt{\left(1 + \left(\frac{r}{\omega}\right)^2 + 2\frac{t}{\tau_D}\right)}} \right) \quad (3.14)$$

where $\tau_D^{(i)} = \frac{\omega_i^2}{4D}$.

FRAP Models on $[-l, l]$ with Reflective Boundaries (Neumann Boundary Conditions)

For a FRAP model in an interval $2l$ ($\Omega = [-l, l]$), consider

$$\left\{ \begin{array}{l} C_t = DC_{xx} \\ \frac{\partial C(-l, t)}{\partial x} = \frac{\partial C(l, t)}{\partial x} = 0 \\ C(x, 0) = C_i \left[1 - K \exp\left(-\frac{2x^2}{\omega^2}\right) \right] \end{array} \right. \quad (3.15)$$

Apply the method of separation of variables and look for a solution in a form

$$u(x, t) = \phi(x)G(t) \quad (3.16)$$

which satisfies from the PDEs

$$\left\{ \begin{array}{l} \frac{dG}{dt} = -\lambda DG \\ \frac{d^2\phi}{dx^2} = -\lambda\phi \end{array} \right.$$

where λ is the separation constant. This implies $G(t) = ce^{-\lambda Dt}$ for some constant c and

$$\begin{cases} \frac{d^2\phi}{dx^2} = -\lambda\phi \\ \frac{\partial\phi}{\partial x}(-l) = 0 \\ \frac{\partial\phi}{\partial x}(l) = 0 \end{cases}$$

of which solution is $\phi(x) = c_1 \cos \sqrt{\lambda}x + c_2 \sin \sqrt{\lambda}x$ for arbitrary constants c_1 and c_2 for $\lambda > 0$

and $\phi(x) = \bar{c}_1 + \bar{c}_2 x$ for $\lambda = 0$. For $\lambda = 0$, $\frac{\partial\phi}{\partial x}(-l) = \frac{\partial\phi}{\partial x}(l) = 0$ indicate that $\bar{c}_2 = 0$.

For $\lambda = 0$, there is a symmetric solution with respect to $x = 0$, $c_2 = 0$. From the boundary

solution, $\frac{\partial\phi}{\partial x}(\pm l) = \mp \sin \sqrt{\lambda}l = 0$, which implies $\lambda = \left(\frac{k\pi}{l}\right)^2$, $k = 1, 2, 3, \dots$. Therefore any linear

combination of $\phi_k(x)G_k(t)$ is the solution, where

$$\begin{cases} G_k(t) = \exp\left(-\frac{k\pi}{l}Dt\right) \\ \phi_k(x) = c_1 \cos\left(\frac{k\pi x}{l}\right) \end{cases} \quad (3.17)$$

to satisfy the initial condition

$$u(x, t) = \mathcal{N}_0 + \sum_{k=1}^{\infty} \mathcal{N}_k \cos \frac{k\pi x}{l} \exp\left(-Dt \left[\frac{k\pi}{l}\right]^2\right)$$

where

$$\mathcal{N}_k = \begin{cases} \frac{1}{2l} \int_{-l}^l C(0, x) dx & \text{if } k = 0 \\ \frac{1}{l} \int_{-l}^l C(0, x) \cos \frac{k\pi x}{l} dx & \text{if } k \geq 1 \end{cases}.$$

Since $C(x, 0)$ and $\cos x$ are even functions,

$$C(x, t) = \mathcal{A}_0 + \sum_{k=1}^{\infty} \mathcal{A}_k \cos \phi(k, l) x \exp(-Dt[\phi(k, l)]^2)$$

where

$$\mathcal{A}_k = \begin{cases} \mathcal{N}_0 = \frac{1}{l} \int_0^l C(0, x) dx \\ \mathcal{N}_k = \frac{2}{l} \int_0^l C(0, x) \cos \frac{k\pi x}{l} dx \end{cases} \quad (3.18)$$

Therefore, when $\phi(k, l) = \frac{k\pi}{l}$,

$$\begin{aligned} F(t) &= q \int_{-r}^r [\mathcal{E} I_0 g_r(x) / \bar{g}] C(x, t) dx \\ &= \frac{q \mathcal{E} I_0 C_i}{\bar{g}} \int_0^l g_r(x) [\mathcal{A}_0 + \sum_{k=1}^{\infty} \mathcal{A}_k \cos \phi(k, l) \exp(-Dt[\phi(k, l)]^2)] dx \\ &= \frac{1}{\bar{g}} \left[\mathcal{A}_0 \int_0^l g_r(x) dx + \sum_{k=1}^{\infty} \mathcal{A}_k \exp(-Dt[\phi(k, l)]^2) \int_0^l g(x) \cos \phi(k, l) dx \right] \\ &= \mathcal{A}_0 + \sum_{k=1}^{\infty} \mathcal{A}_k \exp(-Dt[\phi(k, l)]^2) \int_{-r}^r \frac{g(x)}{\bar{g}} \cos \phi(k, l) dx \\ &= \mathcal{A}_0 + \sum_{k=1}^{\infty} \mathcal{A}_k \mathcal{C}_k \exp(-Dt[\phi(k, l)]^2) \end{aligned} \quad (3.19)$$

where $\mathcal{C}_k = \int_{-r}^r \frac{g(x)}{\bar{g}} \cos \phi(k, l) dx$.

FRAP Models on a Circle \mathbb{S}^1

The FRAP model on a circle with a radius r can be derived by considering the Neumann condition. The FRAP equation about $-\pi\rho < x < \pi\rho$ with Neumann boundary conditions on $x = \pm\pi\rho$ can be derived. If $l = \pi\rho$, then the boundary condition can be described as:

$$\begin{cases} C(-l, t) = C(l, t) \\ \frac{\partial C(-l, t)}{\partial x} = \frac{\partial C(l, t)}{\partial x} \end{cases}$$

Considering the initial condition $C(x, 0)$, the general solution is obtained using the method of separation of variables by linear combination of all product solutions:

$$C_t = \frac{D}{\rho^2} C_{\theta\theta} \quad (3.20)$$

$$\begin{aligned} C(x, t) = a_0 + \sum_{k=1}^{\infty} a_m \cos \frac{k\pi x}{l} \exp \left(-Dt \left[\frac{k\pi}{l} \right]^2 \right) \\ + \sum_{k=1}^{\infty} b_n \sin \frac{k\pi x}{l} \exp \left(-Dt \left[\frac{k\pi}{l} \right]^2 \right). \end{aligned} \quad (3.21)$$

Let the Fourier expansion of the initial condition, $C(x, 0) = g_{\omega}(x)$ be

$$g_{\omega}(x) = a_0 + \sum_{k=1}^{\infty} a_m \cos \frac{k\pi x}{l} + \sum_{k=1}^{\infty} b_n \sin \frac{k\pi x}{l}$$

where

$$\begin{cases} a_0 = \frac{1}{2l} \int_{-l}^l C(x, 0) dx \\ a_m = \frac{1}{l} \int_{-l}^l C(x, 0) \cos \frac{k\pi x}{l} dx \\ b_n = \frac{1}{l} \int_{-l}^l C(x, 0) \sin \frac{k\pi x}{l} dx \end{cases}$$

Therefore

$$\begin{aligned} C(x, t) = a_0 + \sum_{k=1}^{\infty} a_m \cos \frac{k\pi x}{l} \exp \left(-Dt \left[\frac{k\pi}{l} \right]^2 \right) \\ + \sum_{k=1}^{\infty} b_n \sin \frac{k\pi x}{l} \exp \left(-Dt \left[\frac{k\pi}{l} \right]^2 \right). \end{aligned} \quad (3.22)$$

But, since $g_{\omega}(x)$ is an even function,

$$\begin{aligned} a_m &= \frac{1}{l} \int_{-l}^l C(x, 0) \cos \frac{k\pi x}{l} dx \\ &= \frac{1}{2l} \int_0^l C(x, 0) \cos \frac{k\pi x}{l} dx \end{aligned}$$

and

$$b_n = \frac{1}{l} \int_{-l}^l C(x, 0) \sin \frac{k\pi x}{l} dx = 0$$

Therefore

$$C(x, t) = a_0 + \sum_{k=1}^{\infty} a_m \cos \frac{k\pi x}{l} \exp \left(-Dt \left[\frac{k\pi}{l} \right]^2 \right). \quad (3.23)$$

By substituting $l = \pi\rho$

$$C(x, t) = a_0 + \sum_{k=1}^{\infty} a_m \cos \frac{kx}{\rho} \exp \left(-Dt \left[\frac{k}{\rho} \right]^2 \right)$$

With the Gaussian laser profile centered at $x = 0$ of $I_r(x) = \frac{l_0}{g} g_r(x)$ where

$g_r(x) = \exp \left(-\frac{2x^2}{r^2} \right)$ and $\bar{g} = \frac{r}{\sqrt{2/\pi}} \operatorname{erf} \left(\frac{l\sqrt{2}}{r} \right)$, by substituting Eqn. (3.23) and $I_r(x)$, the FRAP

model for a circle is obtained as

$$\begin{aligned} F(t) &= q \int_0^l [\mathcal{E} I_0 g(x) / \bar{g}] C(x, t) dx \\ &= \frac{q \mathcal{E} I_0 c_i}{\bar{g}} \int_0^l g(x) \left[a_0 + \sum_{k=1}^{\infty} a_m \cos \frac{kx}{\rho} \exp \left(-Dt \left[\frac{k}{\rho} \right]^2 \right) \right] dx \\ &= \frac{1}{\bar{g}} \left[a_0 \int_0^l g(x) dx + \sum_{k=1}^{\infty} a_m \exp \left(-Dt \left[\frac{k}{\rho} \right]^2 \right) \int_0^l g(x) \cos \frac{kx}{\rho} dx \right] \\ &= a_0 + \sum_{k=1}^{\infty} a_m \exp \left(-Dt \left[\frac{k}{\rho} \right]^2 \right) \int_0^l g(x) \cos \frac{kx}{\rho} dx \\ &= a_0 + \sum_{k=1}^{\infty} a_m C_k \exp \left(-Dt \left[\frac{k}{\rho} \right]^2 \right) \end{aligned} \quad (3.24)$$

where $C_k = \int_0^l g(x) \cos \frac{kx}{\rho} dx$.

FRAP Models on a Disk \mathbb{D}^2

To consider the diffusion equation in a disc with radius ρ , convert the 2D diffusion equation to the polar coordinate system ($x = \gamma \cos \theta$, $y = \gamma \sin \theta$)

$$\frac{\partial C}{\partial t} = \frac{1}{\gamma} \frac{\partial}{\partial \gamma} \left(\gamma D \frac{\partial C}{\partial \gamma} \right)$$

For boundary condition $C(\rho, t) = C_\infty$, by letting $c = C - C_\infty$,

$$\left\{ \begin{array}{l} \frac{\partial c}{\partial t} = D \left(\frac{\partial^2 c}{\partial \gamma^2} + \frac{1}{\gamma} \frac{\partial c}{\partial \gamma} \right) \\ c(1, t) = 0 \\ c(\gamma, 0) = C(\gamma, 0) - C_\infty. \end{array} \right.$$

When $v(\gamma)e^{-D\beta^2 t} = c$ (method of separation of variables) then v satisfies

$$\frac{\partial^2 v}{\partial \gamma^2} + \frac{1}{\gamma} \frac{\partial v}{\partial \gamma} + \beta^2 v = 0$$

which is Bessel's equation of order zero. Again, since the bounded solution is the goal, the Bessel's function of the second kind, which is infinite at $\gamma = 0$ is ruled out. The Bessel's function of the first kind should satisfy the initial condition,

$$J_0(\beta\rho) = 0.$$

This Bessel function has monotone increasing infinite number of real positive roots,

$\beta_1, \beta_2, \beta_3, \dots$ By the principle of superposition,

$$v(\gamma) = \sum_{n=1}^{\infty} A_n J_0(\alpha_n \gamma)$$

$$c(\gamma, t) = \sum_{n=1}^{\infty} A_n J_0(\alpha_n \gamma) e^{-D\alpha_n^2 t}$$

where A_n is computed from the initial condition using orthogonality of the Bessel's function:

$$\int_0^\rho \gamma J_0(\beta_n \gamma) J_0(\beta_m \gamma) d\gamma = \frac{\rho^2}{2} J_1^2(\beta_n \rho) \delta_{m,n}$$

where $\delta_{m,n}$ is the Dirac delta function. At $t = 0$,

$$\sum_{n=1}^{\infty} A_n J_0(\beta_n \gamma) = C(\gamma, 0) - C_\infty$$

$$\begin{aligned} A_n \frac{\rho^2}{2} J_1^2(\beta_n \rho) &= \int_0^\rho \xi (C(\xi, 0) - C_\infty) J_0(\beta_n \xi) d\xi \\ &= \int_0^\rho \xi C(\xi, 0) J_0(\beta_n \xi) d\xi - C_\infty \int_0^\rho \xi J_0(\beta_n \xi) d\xi \\ &= \int_0^\rho \xi C(\xi, 0) J_0(\beta_n \xi) d\xi - \frac{C_\infty \rho}{\alpha_n} J_1(\beta_n \rho) \\ A_n &= \frac{2}{\rho^2 J_1^2(\beta_n \rho)} \int_0^\rho \xi C(\xi, 0) J_0(\beta_n \xi) d\xi - \frac{2C_\infty}{\beta_n \rho J_1(\beta_n)} \end{aligned}$$

where $\int_0^\rho \gamma J_0(\beta_n \gamma) d\gamma = \frac{\rho}{\beta_n} J_1(\beta_n \rho)$ from $\frac{d}{dx}(x J_1(x)) = x J_0(x)$.

Therefore,

$$\begin{aligned} c(\gamma, t) &= \sum_{n=1}^{\infty} \left(\frac{2}{\rho^2 J_1^2(\beta_n \rho)} \int_0^\rho \xi C(\xi, 0) J_0(\beta_n \xi) d\xi - \frac{2C_\infty}{\beta_n \rho J_1(\beta_n)} \right) J_0(\beta_n \gamma) e^{-D\beta_n^2 t} \\ &= -C_\infty \sum_{n=1}^{\infty} \frac{2J_0(\beta_n \gamma) e^{-D\beta_n^2 t}}{\beta_n \rho J_1(\beta_n \rho)} + \sum_{n=1}^{\infty} \frac{2J_0(\beta_n \gamma) e^{-D\beta_n^2 t}}{\rho^2 J_1^2(\beta_n \rho)} \int_0^\rho \xi C(\xi, 0) J_0(\beta_n \xi) d\xi \end{aligned}$$

From $C(\gamma, t) = C_\infty + c$

$$\begin{aligned}
C(\gamma, t) = C_\infty & \left(1 - \frac{2}{\rho} \sum_{n=1}^{\infty} \frac{J_0(\beta_n \gamma) e^{-D\beta_n^2 t}}{\beta_n J_1(\beta_n \rho)} \right) \\
& + \frac{2}{\rho^2} \sum_{n=1}^{\infty} \frac{J_0(\beta_n \gamma) e^{-D\beta_n^2 t}}{J_1^2(\beta_n \rho)} \int_0^\rho \xi C(\xi, 0) J_0(\beta_n \xi) d\xi
\end{aligned} \tag{3.25}$$

where $J_i, i = 1, 2$ are the Bessel function of the first kind and α_n is the positive roots of

$$J_1(\alpha_n \rho) = 0$$

The Bessel function is the solution to the differential equation below and are nonsingular at origin.

$$x^2 \frac{d^2 y}{dx^2} + x \frac{dy}{dx} + (x^2 - m^2)y = 0 \tag{3.26}$$

The Frobenius Method is used to find this solution. Using the series solution,

$$y = x^k \sum_{n=0}^{\infty} a_n x^n = \sum_{n=0}^{\infty} a_n x^{n+k} \tag{3.27}$$

Substituting Eqn. (3.27) into Eqn. (3.26)

$$\begin{aligned}
& x^2 \sum_{n=0}^{\infty} (k+n)(k+n-1) a_n x^{n+k-2} + x \sum_{n=0}^{\infty} (k+n) a_n x^{n+k-1} + x^2 \sum_{n=0}^{\infty} a_n x^{n+k} \\
& - m^2 \sum_{n=0}^{\infty} a_n x^{n+k} = 0 \\
& \sum_{n=0}^{\infty} (k+n)(k+n-1) a_n x^{n+k} + \sum_{n=0}^{\infty} (k+n) a_n x^{n+k} + \sum_{n=2}^{\infty} a_{n-2} x^{n+k} - m^2 \sum_{n=0}^{\infty} a_n x^{n+k} \\
& = 0
\end{aligned}$$

When $n = 0$,

$$a_0[k(k-1) + k - m^2] = a_0(k^2 - m^2) = 0$$

Since a_0 is the first nonzero term, $k^2 - m^2 = 0$. Thus, $k = \pm m$

Now, fluorescence equation yields

$$\begin{aligned}
F(t) &= q \iint_{\mathbb{D}} [\varepsilon I_r(x, y)] C(x, y, t) dx dy \\
&= q \int_0^{2\pi} \int_0^\rho [\varepsilon I_r(\gamma)] C(\gamma, t) \gamma d\gamma d\theta \\
&= q \int_0^{2\pi} \int_0^\rho [\varepsilon I_0 \frac{g_r(\gamma)}{\bar{g}}] C_\infty \left(1 - \frac{2}{\rho} \sum_{n=1}^{\infty} \frac{J_0(\beta_n \gamma) e^{-D\beta_n^2 t}}{\beta_n J_1(\beta_n \rho)} \right) d\gamma d\theta \\
&+ q \int_0^{2\pi} \int_0^\rho \left[\varepsilon I_0 \frac{g_r(\gamma)}{\bar{g}_r} \right] \frac{2}{\rho^2} \sum_{n=1}^{\infty} \exp(-D\beta_n^2 t) \frac{J_0(\gamma \beta_n)}{J_1^2(\rho \beta_n)} \int_0^\rho \xi C(\xi, 0) J_0(\xi \beta_n) d\xi \\
&= \frac{q \varepsilon I_0 C_\infty(2\pi)}{\bar{g}_r} \left(\int_0^\rho g_r(\gamma) d\gamma - \frac{2}{\rho} \sum_{n=1}^{\infty} \frac{\exp(-D\beta_n^2 t)}{\beta_n} \frac{\int_0^\rho g_r(\gamma) J_0(\gamma \beta_n) d\gamma}{J_1(\rho \beta_n)} \right) d\gamma \\
&+ \frac{q \varepsilon I_0(2\pi)}{\bar{g}_r} \cdot \frac{2}{\rho^2} \sum_{n=1}^{\infty} \exp(-D\beta_n^2 t) \frac{\int_0^\rho g_r(\gamma) J_0(\gamma \beta_n) d\gamma}{J_1^2(\rho \beta_n)} \int_0^\rho \xi C(\xi, 0) J_0(\xi \alpha_n) d\xi \\
&= F_\infty \left(1 - \frac{2}{\rho} \sum_{n=1}^{\infty} \frac{\exp(-D\beta_n^2 t)}{\beta_n J_1(\rho \beta_n)} \mathcal{R}_n \right) + \frac{4\pi}{\rho^2} \sum_{n=1}^{\infty} \frac{\exp(-D\beta_n^2 t)}{J_1^2(\rho \beta_n)} \mathcal{W}_n \mathcal{R}_n \quad (3.28)
\end{aligned}$$

where

$$\begin{cases} \mathcal{R}_n = \frac{2\pi}{\bar{g}} \int_0^\rho g_r(\gamma) J_0(\gamma \beta_n) d\gamma \\ \mathcal{W}_n = \int_0^\rho \xi C(\xi, 0) J_0(\xi \alpha_n) d\xi \end{cases}$$

FRAP models on a sphere (\mathbb{S}^2)

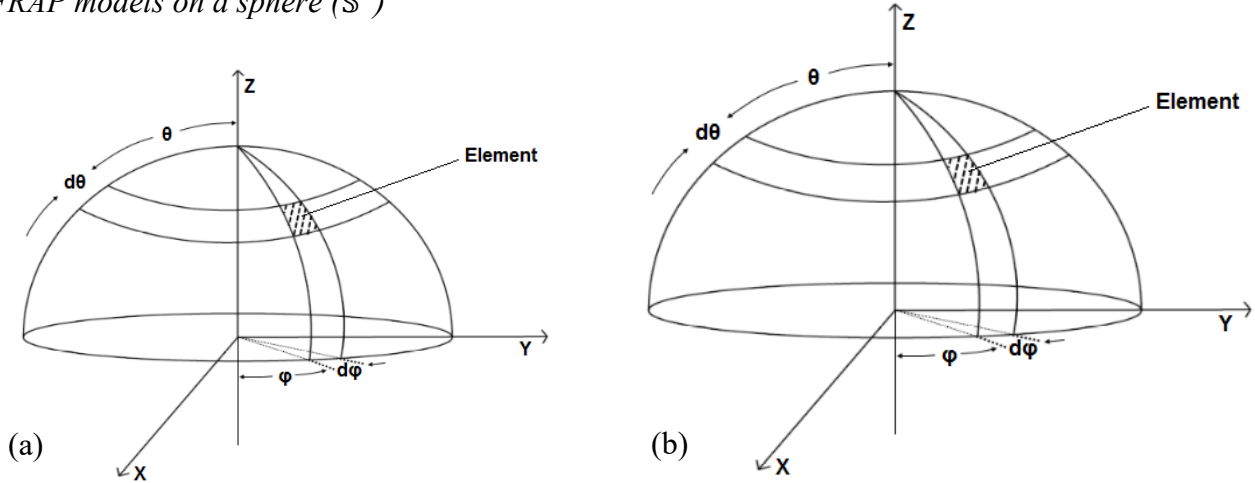


Fig. 6. Pictorial view of spherical coordinates

The Laplacian in the Cartesian coordinate system can be represented in the spherical coordinate system as

$$\Delta_x = \Delta_r + \frac{1}{r^2} \Delta_{(\theta, \varphi)} \quad (3.29)$$

where

$$\Delta_r = \frac{1}{r^2} \frac{\partial}{\partial r} \left(r^2 \frac{\partial}{\partial r} \right)$$

$$\Delta_{(\theta, \varphi)} = \frac{1}{\sin \theta} \frac{\partial}{\partial \theta} \left(\sin \theta \frac{\partial}{\partial \theta} \right) + \frac{1}{\sin^2 \theta} \frac{\partial^2}{\partial \varphi^2}$$

Therefore, the diffusion equation in spherical coordinates $(r \sin \theta \cos \varphi, r \sin \theta \sin \varphi, r \cos \theta)$ is:

$$C_t = D \left[\frac{1}{r^2} \frac{\partial}{\partial r} \left(r^2 \frac{\partial C}{\partial r} \right) + \frac{1}{r^2 \sin \theta} \frac{\partial}{\partial \theta} \left(\sin \theta \frac{\partial C}{\partial \theta} \right) + \frac{1}{r^2 \sin^2 \theta} \frac{\partial^2 C}{\partial \varphi^2} \right] \quad (3.30)$$

for $0 \leq \theta \leq \pi$ and $0 \leq \varphi \leq 2\pi$.

In particular, the diffusion equation on the sphere surface with radius ρ is $\left(\frac{\partial u}{\partial r} = 0 \right)$

$$\frac{\partial C}{\partial t} = \frac{D}{\rho^2} \left[\frac{1}{\sin \theta} \frac{\partial}{\partial \theta} \left(\sin \theta \frac{\partial C}{\partial \theta} \right) + \frac{1}{\sin^2 \theta} \frac{\partial^2 C}{\partial \phi^2} \right]$$

Apply the method of separation of variables and look for a solution in a form $C(t, \theta, \varphi) = G(t)Y(\theta, \varphi)$. By separation of variables,

$$\begin{cases} \frac{dG}{dt} = -\lambda \frac{D}{\rho^2} G \\ \frac{1}{\sin \theta} \frac{\partial}{\partial \theta} \left(\sin \theta \frac{\partial Y}{\partial \theta} \right) + \frac{1}{\sin^2 \theta} \frac{\partial^2 Y}{\partial \phi^2} = -\lambda Y \end{cases} \quad (3.31)$$

The first equation provides $G(t) = \exp\left(-\lambda \frac{Dt}{\rho^2}\right)$. The second equation can be solved by the spherical harmonic functions, Y_{lm} which satisfies

$$\frac{1}{\sin \theta} \frac{\partial}{\partial \theta} \left(\sin \theta \frac{\partial Y_{lm}}{\partial \theta} \right) + \frac{1}{\sin^2 \theta} \frac{\partial^2 Y_{lm}}{\partial \phi^2} = -l(l+1)Y_{lm}$$

where $|m| \leq l$ and $l \geq 0$ for $\lambda = l(l+1)$. In particular, considering the solution symmetric with respect to rotation about z-axis, it requires that Y_{lm} is a function of $\cos \theta$. By representing Y_{lm} in terms of the Legendre polynomials,

$$Y_{lm}(\varphi, \theta) = \sqrt{\frac{2l+1}{4\pi} \cdot \frac{(l-m)!}{(l+m)!}} P_l^m(\cos \theta) e^{im\varphi} \quad (3.32)$$

Since the diffusion is radial from the north pole, the solution should be independent on φ and have $m = 0$. Y_{l0} is called zonal harmonic and forms a complete orthonormal set in $L^2(\mathbb{S}^2)$:

$$Y_{l0}(\varphi, \theta) = \sqrt{\frac{2l+1}{4\pi}} P_l^0(\cos \theta)$$

The Green's function for the problem is given by [52]

$$\begin{aligned} \Psi(\phi, \theta) &= \sum_{l=0}^{\infty} \sqrt{\frac{2l+1}{4\pi}} Y_{l0}(\phi, \theta) \exp\left(\frac{-l(l+1)Dt}{\rho^2}\right) \\ &= \sum_{l=0}^{\infty} \left(\frac{2l+1}{4\pi}\right) P_l^0(\cos \theta) \exp\left(\frac{-l(l+1)Dt}{\rho^2}\right) \end{aligned} \quad (3.33)$$

which is often referred as the Gauss-Weierstrass Kernel and the spherical harmonics of degree l (Y_{lm}) are defined as

$$Y_{lm} = \sqrt{\frac{2l+1}{4\pi} \cdot \frac{(l-m)!}{(l+m)!}} P_l^m(\cos \theta) e^{-im\phi} \quad (3.34)$$

for the Legendre polynomials of order m ,

$$\left\{ \begin{array}{l} P_l^m(x) = \frac{(1-x^2)^{m/2}}{2^l l!} \frac{d^{(l+m)}}{dx^{(l+m)}} (x^2-1)^l \\ P_l^0(x) = \frac{1}{2^l l!} \frac{d^l}{dx^l} (x^2-1)^l \end{array} \right.$$

Putting the solutions for G and Y together, the solution can be represented as an infinite series of the Gauss-Weierstrass Kernel:

$$\begin{aligned} C(\varphi, \theta, t) &= \sum_{l=0}^{\infty} \mathcal{Y}_l \sqrt{\frac{2l+1}{4\pi}} Y_{l0}(\varphi, \theta) \exp\left(-\frac{l(l+1)}{\rho^2} Dt\right) \\ &= \sum_{l=0}^{\infty} \mathcal{Y}_l \left(\frac{2l+1}{4\pi}\right) P_l^0(\cos \theta) \exp\left(-\frac{l(l+1)}{\rho^2} Dt\right) \end{aligned} \quad (3.35)$$

for some constants \mathcal{Y}_l to be determined by the initial condition. The initial condition on the sphere is symmetric with respect to φ and therefore a function of $\rho\theta$

$$\begin{aligned} I_r(\phi, \theta) &= \frac{I_0}{\bar{g}} \exp\left(-\frac{2\rho^2\theta^2}{r^2}\right) \\ \bar{g} &= \int_0^\pi \exp\left(-\frac{2\rho^2\theta^2}{r^2}\right) d\theta \\ &= \sqrt{\frac{\pi}{2}} \operatorname{erf}\left(\frac{\rho}{r} \sqrt{2\pi}\right) \end{aligned}$$

$$C(\varphi, \theta, 0) = C_i \left[1 - K \exp\left(-\frac{2\rho^2\rho^2\theta^2}{\omega^2}\right)\right]$$

where $\operatorname{erf}(x) = \frac{2}{\sqrt{\pi}} \int_0^x e^{-t^2} dt$. At $t = 0$ for $C(\varphi, \theta, t)$

$$\begin{aligned}
C(\varphi, \theta, 0) &= \sum_{l=0}^{\infty} \mathcal{Y}_l \left(\frac{2l+1}{4\pi} \right) P_l^0(\cos \theta) \\
&= C_i \left[1 - K \exp \left(-\frac{2\rho^2 \rho^2 \theta^2}{\omega^2} \right) \right]
\end{aligned} \tag{3.36}$$

By using the orthogonality property:

$$\begin{aligned}
&\int_0^{2\pi} \int_0^\pi \left(\frac{2l+1}{4\pi} \right) P_l^0(\cos \theta) P_k^0(\cos \theta) \sin \theta \, d\theta \, d\phi \\
&= 2\pi \left(\frac{2l+1}{4\pi} \right) \int_{-1}^1 P_l^0(x) P_k^0(x) \, dx \\
&= \left(\frac{2l+1}{2} \right) \left(\frac{2}{2l+1} \right) \delta_{lk} \\
\mathcal{Y}_l &= \int_0^{2\pi} \int_0^\pi \left[\sum_{k=1}^{\infty} \mathcal{Y}_k \frac{2k+1}{4\pi} P_l^0(\cos \theta) \right] P_l^0(\cos \theta) \sin \theta \, d\theta \, d\phi \\
&= C(\varphi, \theta, 0) P_l^0(\cos \theta) \sin \theta \, d\theta \, d\phi \\
&= C_i \int_0^{2\pi} \int_0^\pi \left[1 - K \exp \left(-\frac{2\rho^2 \rho^2 \theta^2}{\omega^2} \right) \right] P_l^0(\cos \theta) \sin \theta \, d\theta \, d\phi
\end{aligned}$$

Finally, the FRAP formula can be obtained by the standard calculation

$$\begin{aligned}
F(t) &= q \int_0^{2\pi} \int_0^\pi \left[\varepsilon \frac{I_0}{\bar{g}_r} \exp \left(-\frac{2\rho^2 \sin^2 \frac{\theta}{2}}{r^2} \right) \right] \left[\sum_0^\infty \mathcal{Y}_l \left(\frac{2l+1}{4\pi} \right) P_l^0(\cos \theta) \exp \left(-\frac{l(l+1)}{\rho^2} D_t \right) \right] \sin \theta \, d\theta \, d\phi \\
&= F_i \sum_0^\infty \mathcal{Y}_l \mathcal{P}_l \left(\frac{2l+1}{2} \right) \exp \left(-\frac{l(l+1)}{\rho^2} D_t \right)
\end{aligned} \tag{3.37}$$

where

$$\mathcal{P}_l = \int_0^{2\pi} \int_0^\pi \left[\frac{I_0}{\bar{g}} \exp \left(-\frac{2\rho^2 \theta^2}{r^2} \right) P_l^0(\cos \theta) \right] \sin \theta \, d\theta \, d\phi$$

The other cases can be considered in a similar way. Table 1 summarizes all the FRAP models covered in this study.

Coding Results and Graph

The MATLAB software was used to write the codes for some FRAP models that were derived in this chapter. Since they are FRAP models, they virtually have to give very similar graphs. Variables used can be tweaked to give the user the preferred adjustments to match with his or her experiments.

Algorithm for \mathbb{R}^1 Model

The following are the steps for \mathbb{R}^1 Model:

- Assign values to the pre-bleach fluorescence intensity (F_i), diffusion coefficient (D), radial distance (r), half width at e^{-2} intensity (ω), and depth of the bleaching parameter (K).
 - Calculate the characteristic diffusion time (τ_D).
- For time $t = 1$ to 20 at intervals of 0.1.
 - Calculate the fluorescence intensity.
- Plot a graph of time against fluorescence intensity.

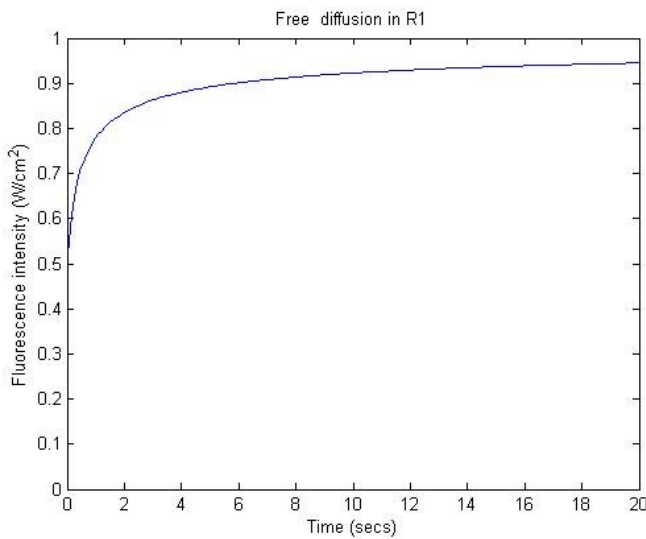


Fig. 7. 1D FRAP Recovery Curve.

Algorithm for \mathbb{R}^2 and \mathbb{R}^N Model

The algorithm for the FRAP model for both \mathbb{R}^2 and \mathbb{R}^N is very similar to the algorithm used in one dimensional FRAP analysis. The only changes would be to the fluorescence intensity formulas.

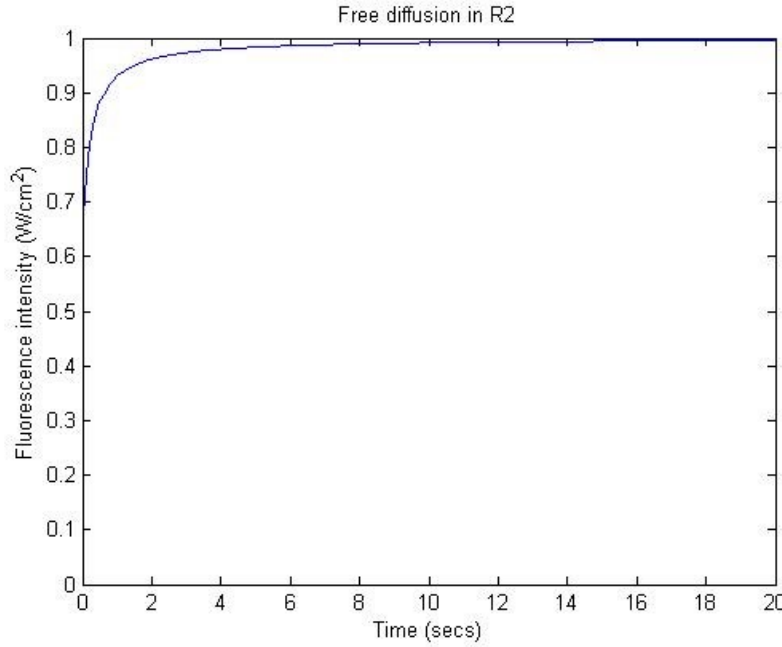


Fig. 8. FRAP Recovery Curve in \mathbb{R}^2

Algorithm for Finite Interval Model using Neumann Boundary Condition

The following are the steps for the finite interval using Neumann condition:

- Assign values to the pre-bleach fluorescence intensity (F_i), diffusion coefficient (D), radial distance (r), half width at e^{-2} intensity (ω), depth of the bleaching parameter (K), and t from 0 to 10.
 - Calculate C_0 and N_0

- Let y be empty
- Let $psum = N_0$
- For $k = 1$ to 50 at intervals of 0.1
 - Calculate λ_k
 - Calculate N_k and E_k using λ_k

End

- $y = psum$
- Plot a graph of time against

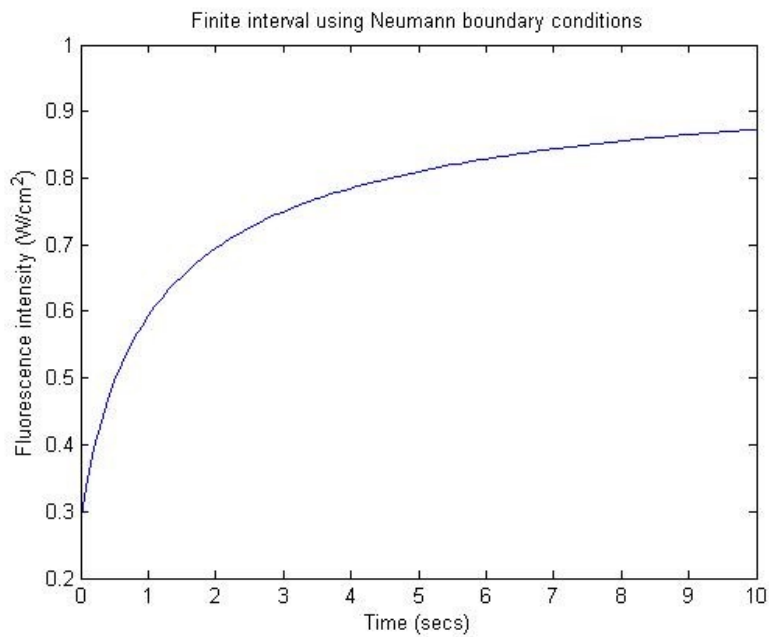


Fig. 9. FRAP curve of a finite domain with Neumann boundary condition

Algorithm for Finite Interval Model using Dirichlet Boundary Condition

The following are the steps for the Finite Interval using Dirichlet Condition:

- Assign values to the pre-bleach fluorescence intensity (F_i), diffusion coefficient (D), radial distance (r), half width at e^{-2} intensity (ω), depth of the bleaching parameter (K), t from 0 to 10 and x from -1 to 1 with intervals of 0.1.
 - Calculate C_0 where C_∞ is an assigned value.
 - Let y be empty.
 - Let psum = 0.
- For $k = 1$ to 50 at intervals of 0.1.
 - Calculate λ_k .
 - Calculate D_k and O_k using λ_k .
 - Find new psum.
- End.
- $y = C_\infty + \text{psum}$.
- Plot a graph of time against y .

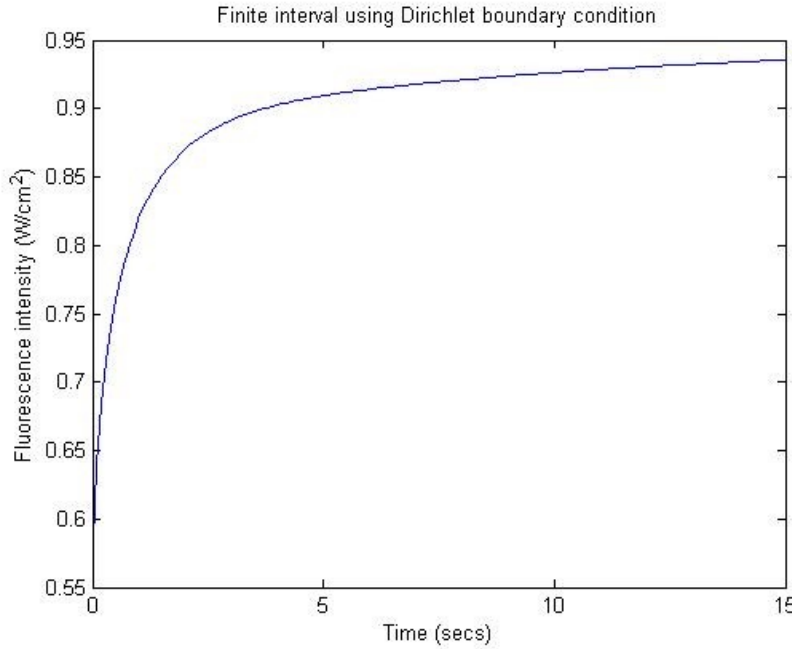


Fig. 10. FRAP curve of a finite domain with Dirichlet boundary condition.

Algorithm for Disk Model using Neumann Boundary Condition

The following are the steps for the disk using Neumann condition:

- Assign values to diffusion coefficient (D), radial distance (r), half width at e^{-2} intensity (ω), and depth of the bleaching parameter (K), t from 0 to 10 and rho (ρ).
 - Assign random values to A_n .
 - Calculate a_n .
 - Calculate \bar{g} , g and set variable $SW_k = 0$.
- For n from 1 to 30,
 - Find R_n by integrating the Bessel function.
 - Let $SW_{nk} = 0$.
- For k from 0 to 20,
 - Find g_r and new SW_{nk} .

- End
- Now find new psum
- End
- Plot time against fluorescence intensity

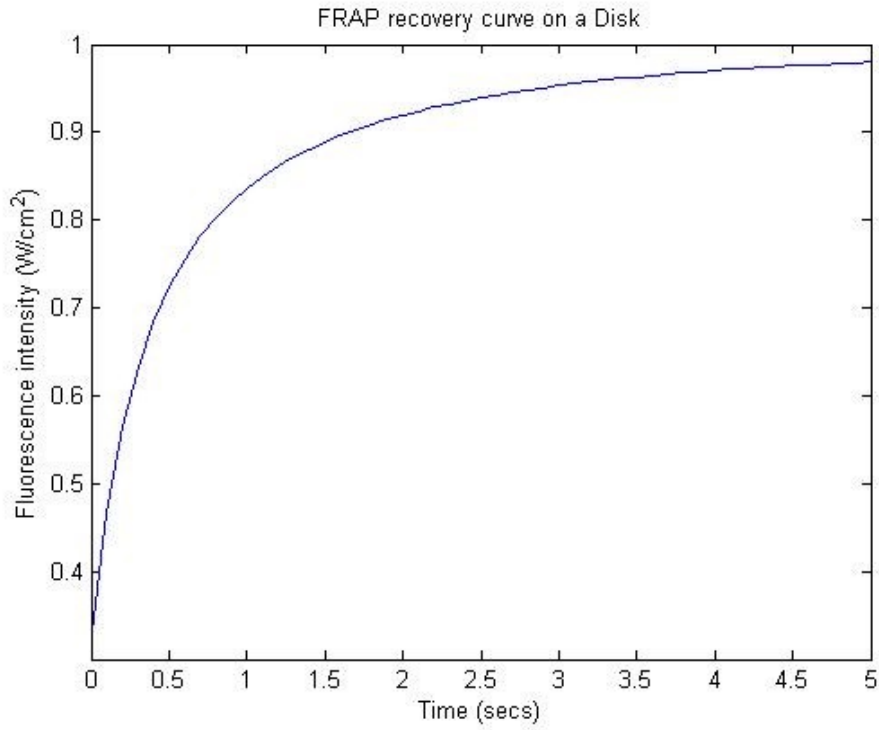


Fig. 11. FRAP curve of a disk with Neumann boundary condition

Table 1. FRAP models for different geometries

	FRAP MODEL FORMULAS						
SPACE	\mathbb{R}^1	\mathbb{R}^2	\mathbb{R}^N	\mathbb{S}^1	\mathbb{S}^2	\mathbb{D}^2	$[-l, l]$
KINETICS	(3.3)	(3.3)	(3.3)	(3.20)	(3.30)	(3.25)	(3.3)
BOUNDARY CONDITIONS	NA	NA	NA	Periodic Boundary	NA	Neumann	Neumann/ Dirichlet
FRAP EQUATION	(3.9)	(3.11)	(3.14)	(3.24)	(3.37)	(3.28)	(3.19)

Chapter 4

CONCLUSION

This thesis derived FRAP models in various geometries for free diffusion that are applicable to both conventional and confocal FRAP. Conventional FRAP developed by Axelrod et al. used its equations to fit FRAP recovery curves that consists of measuring the fluorescence intensity change in a diffraction-limited spot following photobleaching with a Gaussian-profiled laser [53]. He assumed that the bleaching event is far faster than diffusion, and there are no data involving the spatial distribution of bleached molecules outside the bleach spot is needed.

These assumptions do not apply to FRAP experiments with CLSM, especially for soluble proteins. Confocal FRAP involves the use of laser scanning confocal microscopes, which makes use of a single laser for bleaching and imaging. Thus, there is enough time to allow for diffusion when scanning the bleach region [54]. This intrinsic property is addressed by developing a formalism [53], [54] that can be used to correct for diffusion during photobleaching, which has the same form as the diffusion FRAP model of Axelrod [53].

Here, this formalism was extended [54] to incorporate both diffusion and binding events during photobleaching, so that the models are equally applicable to both conventional and confocal FRAP. To maximize the usefulness of this approach, a series of FRAP models were derived on various geometries, which are potentially important in a physiological application point of view. Researchers can test this model to measure various GFPs in solutions of varying viscosities to estimate D . Their diffusion coefficients obtained should not be so different from that of the Stoke-Einstein equation. Some small variations might come due to experimental variables like the bleach spot size or number of scans used to bleach the spot. It is important for

the right model to be selected in order to receive the right results. This formalism can also be explored and used to develop reaction diffusion and dissociation models with respect to different geometries.

REFERENCES

1. L. R. Solon, R. Aronson, and G. Gould, "Physiological implications of laser beams," *Science*, vol. 134, pp. 1506–1508, Nov 1961.
2. A. Einstein, "On the quantum theory of radiation," *Physikalische Zeitschrift*, vol. 18, pp. , 121â128, 1917.
3. M. Chalfie and M. Chalfie, "GFP: lighting up life (Nobel Lecture)," *Angew. Chem. Int. Ed. Engl.*, vol. 48, no. 31, pp. 5603–5611, 2009.
4. O. Shimomura, F. H. Johnson, and Y. Saiga, "Extraction, purification and properties of aequorin, a bioluminescent protein from the luminous hydromedusan, *Aequorea*," *J Cell Comp Physiol*, vol. 59, pp. 223–239, Jun 1962.
5. O. Shimomura and O. Shimomura, "Discovery of green fluorescent protein (GFP) (Nobel Lecture)," *Angew. Chem. Int. Ed. Engl.*, vol. 48, no. 31, pp. 5590–5602, 2009.
6. M. Chalfie, Y. Tu, G. Euskirchen, W. W. Ward, and D. C. Prasher, "Green fluorescent protein as a marker for gene expression," *Science*, vol. 263, pp. 802–805, Feb 1994.
7. R. Y. Tsien, "The green fluorescent protein," *Annu. Rev. Biochem.*, vol. 67, pp. 509–544, 1998.
8. G. Carrero, E. Crawford, M. J. Hendzel, and G. de Vries, "Characterizing fluorescence recovery curves for nuclear proteins undergoing binding events," *Bull. Math. Biol.*, vol. 66, pp. 1515–1545, Nov 2004.
9. P. Hinow, C. E. Rogers, C. E. Barbieri, J. A. Pietenpol, A. K. Kenworthy, and E. DiBenedetto, "The DNA binding activity of p53 displays reaction-diffusion kinetics," *Biophys. J.*, vol. 91, pp. 330–342, Jul 2006.

10. G. Carrero, D. McDonald, E. Crawford, G. de Vries, and M. J. Hendzel, "Using FRAP and mathematical modeling to determine the in vivo kinetics of nuclear proteins," *Methods*, vol. 29, pp. 14–28, Jan 2003.
11. R. D. Phair, P. Scaffidi, C. Elbi, J. Vecerova, A. Dey, K. Ozato, D. T. Brown, G. Hager, M. Bustin, and T. Misteli, "Global nature of dynamic protein-chromatin interactions in vivo: three-dimensional genome scanning and dynamic interaction networks of chromatin proteins," *Mol. Cell. Biol.*, vol. 24, pp. 6393–6402, Jul 2004.
12. R. Peters, J. Peters, K. H. Tews, and W. Bahr, "A microfluorimetric study of translational diffusion in erythrocyte membranes," *Biochim. Biophys. Acta*, vol. 367, pp. 282–294, Nov 1974.
13. D. Axelrod, D. E. Koppel, J. Schlessinger, E. Elson, and W. W. Webb, "Mobility measurement by analysis of fluorescence photobleaching recovery kinetics," *Biophys. J.*, vol. 16, pp. 1055–1069, Sep 1976.
14. D. M. Soumpasis, "Theoretical analysis of fluorescence photobleaching recovery experiments," *Biophys. J.*, vol. 41, pp. 95–97, Jan 1983.
15. J. C. G. Blonk, A. Don, H. Van Aalst, and J. J. Birmingham, "Fluorescence photobleaching recovery in the confocal scanning light microscope," *Journal of Microscopy*, vol. 169, no. 3, pp. 363–374, 1993.
16. K. Braeckmans, L. Peeters, N. N. Sanders, S. C. De Smedt, and J. Demeester, "Three-dimensional fluorescence recovery after photobleaching with the confocal scanning laser microscope," *Biophys. J.*, vol. 85, pp. 2240–2252, Oct 2003.

17. P. Wedekind, U. Kubitscheck, and R. Peters, "Scanning microphotolysis: a new photobleaching technique based on fast intensity modulation of a scanned laser beam and confocal imaging.," *J Microsc*, vol. 176, pp. 23–33, Oct 1994.
18. J. Lippincott-Schwartz, E. Snapp, and A. Kenworthy, "Studying protein dynamics in living cells," *Nat. Rev. Mol. Cell Biol.*, vol. 2, pp. 444–456, Jun 2001.
19. J. Lippincott-Schwartz, N. Altan-Bonnet, and G. H. Patterson, "Photobleaching and photoactivation: following protein dynamics in living cells," *Nat. Cell Biol.*, vol. Suppl, pp. 7–14, Sep 2003.
20. K. Jacobson, E. Wu, and G. Poste, "Measurement of the translation mobility of concanavalin a in glycerol-saline solutions and on the cell surface by fluorescence recovery after photobleaching," *Biochimica et Biophysica Acta (BBA) - Biomembranes*, vol. 433, no. 1, pp. 215 – 222, 1976.
21. D. A. Berk, F. Yuan, M. Leunig, and R. K. Jain, "Fluorescence photobleaching with spatial Fourier analysis: measurement of diffusion in light-scattering media," *Biophys. J.*, vol. 65, pp. 2428–2436, Dec 1993.
22. F. Mueller, P. Wach, and J. G. McNally, "Evidence for a common mode of transcription factor interaction with chromatin as revealed by improved quantitative fluorescence recovery after photobleaching," *Biophys. J.*, vol. 94, pp. 3323–3339, Apr 2008.
23. J. Beaudouin, F. Mora-Bermudez, T. Klee, N. Daigle, and J. Ellenberg, "Dissecting the contribution of diffusion and interactions to the mobility of nuclear proteins," *Biophys. J.*, vol. 90, pp. 1878–1894, Mar 2006.
24. M. Kang and A. K. Kenworthy, "A closed-form analytic expression for frap formula for the binding diffusion model," *Biophysical Journal*, vol. 95, no. 2, pp. L13 – L15, 2008.

25. M. Kang, C. A. Day, K. Drake, A. K. Kenworthy, and E. DiBenedetto, "A generalization of theory for two-dimensional fluorescence recovery after photobleaching applicable to confocal laser scanning microscopes," *Biophys. J.*, vol. 97, pp. 1501–1511, Sep 2009.
26. M. Kang, C. A. Day, E. DiBenedetto, and A. K. Kenworthy, "A quantitative approach to analyze binding diffusion kinetics by confocal FRAP," *Biophys. J.*, vol. 99, pp. 2737–2747, Nov 2010.
27. H. Stahlberg, E. Kutejova, K. Suda, B. Wolpensinger, A. Lustig, G. Schatz, A. Engel, and C. K. Suzuki, "Mitochondrial Lon of *Saccharomyces cerevisiae* is a ring-shaped protease with seven flexible subunits," *Proc. Natl. Acad. Sci. U.S.A.*, vol. 96, pp. 6787–6790, Jun 1999.
28. H. Biermann, B. Pietz, R. Dreier, K. W. Schmid, C. Sorg, and C. Sunderkotter, "Murine leukocytes with ring-shaped nuclei include granulocytes, monocytes, and their precursors," *J. Leukoc. Biol.*, vol. 65, pp. 217–231, Feb 1999.
29. D. G. Russell and R. G. Burns, "The polar ring of coccidian sporozoites: a unique microtubule-organizing centre," *J. Cell. Sci.*, vol. 65, pp. 193–207, Jan 1984.
30. M. Koster, T. Frahm, and H. Hauser, "Nucleocytoplasmic shuttling revealed by FRAP and FLIP technologies," *Curr. Opin. Biotechnol.*, vol. 16, pp. 28–34, Feb 2005.
31. M. Chalfie and M. Chalfie, "GFP: lighting up life (Nobel Lecture)," *Angew. Chem. Int. Ed. Engl.*, vol. 48, no. 31, pp. 5603–5611, 2009.
32. T. Cremer and C. Cremer, "Chromosome territories, nuclear architecture and gene regulation in mammalian cells," *Nat. Rev. Genet.*, vol. 2, pp. 292–301, Apr 2001.
33. R. D. Phair and T. Misteli, "High mobility of proteins in the mammalian cell nucleus," *Nature*, vol. 404, pp. 604–609, Apr 2000.

34. T. Pederson, "Diffusional protein transport within the nucleus: a message in the medium," *Nat. Cell Biol.*, vol. 2, pp. E73–74, May 2000.
35. S. R. McRae, Green Fluorescence Protein: Towards Extra Cellular Applications. phdthesis, Griffith University, Dec. 2008.
36. G. Stokes, J. Larmor, and I. Humphry, *Memoir and Scientific Correspondence of the Late Sir George Gabriel Stokes, Bart. ... Memoir and Scientific Correspondence of the Late Sir George Gabriel Stokes, Bart*, University Press, 1907.
37. Wikipedia, "Cell nucleus — wikipedia, the free encyclopedia," 2017. [Online; accessed 31-October-2017].
38. M. Kasha, "50 years of the jablonski diagram," *Acta Physica Polonica A*, vol. 71, pp. 661–670, 1987.
39. E. portal of PDB, "Molecular models: Exploring the structure of fluorescent proteins." Website.
40. F. Cannone, G. Chirico, and A. Diaspro, "Two-photon interactions at single fluorescent molecule level," *J Biomed Opt*, vol. 8, pp. 391–395, Jul 2003.
41. O. Scholz, A. Thiel, W. Hillen, and M. Niederweis, "Quantitative analysis of gene expression with an improved green fluorescent protein," *European Journal of Biochemistry*, vol. 267, no. 6, pp. 1565–1570, 2000.
42. N. Periasamy, S. Bicknese, and A. S. Verkman, "Reversible photobleaching of fluorescein conjugates in air-saturated viscous solutions: singlet and triplet state quenching by tryptophan," *Photochem. Photobiol.*, vol. 63, pp. 265–271, Mar 1996.

43. M. N. Berberan-Santos, ed., *Fluorescence of Supramolecules, Polymers, and Nanosystems*, vol. 04 of *Springer Series on Fluorescence*. Springer Berlin Heidelberg, 2008.
44. R. D. Phair and T. Misteli, “Kinetic modelling approaches to in vivo imaging,” *Nat. Rev. Mol. Cell Biol.*, vol. 2, pp. 898–907, Dec 2001.
45. J. Braga, J. M. Desterro, and M. Carmo-Fonseca, “Intracellular macromolecular mobility measured by fluorescence recovery after photobleaching with confocal laser scanning microscopes,” *Mol. Biol. Cell*, vol. 15, pp. 4749–4760, Oct 2004.
46. D. Mazza, F. Cella, G. Vicidomini, S. Krol, and A. Diaspro, “Role of three-dimensional bleach distribution in confocal and two-photon fluorescence recovery after photobleaching experiments,” *Appl. Opt.*, vol. 46, pp. 7401–7411, Oct 2007.
47. E. A. Reits and J. J. Neefjes, “From fixed to FRAP: measuring protein mobility and activity in living cells,” *Nat. Cell Biol.*, vol. 3, pp. E145–147, Jun 2001.
48. A. Einstein, “Über die von der molekularkinetischen theorie der wärme geforderte bewegung von in ruhenden flüssigkeiten suspendierten teilchen,” *Annalen der Physik*, vol. 322, no. 8, pp. 549–560, 1905.
49. H. S. Carslaw and J. C. Jaeger, *Conduction of Heat in Solids*, ch. The Laplace transformation: problems on the cylinder and sphere, pp. 345–347. Oxford University Press, 1959.
50. T. Bælow, “Spherical diffusion for 3d surface smoothing,” *IEEE Trans. Pattern Anal. Mach. Intell.*, vol. 26(12), pp. 1650–1654, 2004.

51. D. Axelrod, D. Koppel, J. Schlessinger, E. Elson, and W. Webb, "Mobility measurement by analysis of fluorescence photobleaching recovery kinetics.," *Biophys J*, vol. 16, pp. 1055–1069, Sep 1976.
52. M. Weiss, "Challenges and artifacts in quantitative photobleaching experiments.," *Traffic*, vol. 5, pp. 662–671, Sep 2004.
53. J. Braga, J. M. P. Desterro, and M. Carmo-Fonseca, "Intracellular macromolecular mobility measured by fluorescence recovery after photobleaching with confocal laser scanning microscopes.," *Mol Biol Cell*, vol. 15, pp. 4749–4760, Oct 2004.
54. M. Kang, C. A. Day, K. Drake, A. K. Kenworthy, and E. DiBenedetto, "A generalization of theory for two-dimensional fluorescence recovery after photobleaching applicable to confocal laser scanning microscopes.," *Biophys J*, vol. 97, pp. 1501–1511, Sep 2009.

APPENDIX

MATLAB CODES FOR FRAP MODELS

1. FRAP In 1D Code

```

1. D=1;
2. Fi=1;
3. r=1; w=1;
4. %K is the depth of the bleaching parameter
5. K=0.7;
6. Td=(w^2)/(4*D);
7. t=0:0.1:20;
8. F= Fi*( 1-(K./sqrt(1+(r^2)/(w^2)+2*t/Td ) ));
9. plot(t,F);
10. xlim([0,20]);
    ylim([0,1]);

```

2. Code for \mathbb{R}^2

```

11. D=1;
12. Fi=1;
13. r=1;
14. w=1;
15. %K is the depth of the bleaching parameter
16. K=0.7;
17. Td=(w^2)/(4*D);
18. t=0:0.1:1;
19. F= Fi*( 1- (K./(1+ (r^2)/(w^2) +2*t/Td ) ));
20. plot(t,F);
21. xlim([0,20]);
    ylim([0,1]);

```

3. Code for Dirichlet Boundary Condition

```

22. t=[0:1:15];
23. l=5;
24. x=[-l:1:l];
25. D=1;
26. K=0.5;
27. r=1;
28. Coo=.95;
29. c0=exp(-K*exp(-2*x.^2/r/r));
30. y=[];
31. psum=0;
32. N0=trapz(x,c0 )/2/l;
33. for k=1:50
34.     lamdak=(2*k-1)*pi/l/2;
35.     Dk=(-1)^k*4*Coo/(2*k-1)/pi+trapz(x,c0.*cos(lamdak*x))/l;      Ok=trapz(x,exp(-
        2*x.^2/r/r).*cos(lamdak*x))*sqrt(pi/2)/r/erf(1*sqrt(2)/r);      psum=psum+Dk*Ok*exp(-D*t*lamdak^2);
36. end
37. y =Coo+psum;

```

```
38.
    plot(t, y)
```

4. Code for Neumann Boundary Condition

```
39. t=[0:.1:10];
40. l=5;
41. x=[-l:.1:l];
42. D=.5;
43. K=1;
44. r=1;
45. w=1;
46. c0=exp(-K*exp(-2*x.^2/w/w));
47. y=[];
48. N0=trapz(x,c0)/2/l;
49. psum=N0;
50. for k=1:50
51.     lamdak=k*pi/l;
52.     Nk=trapz(x,c0.*cos(lamdak*x))/l;
53.     Ek=trapz(x,exp(-2*x.*x/r/r).*(cos(lamdak*x))*sqrt(pi/2)/r/erf(1*sqrt(2)/r));
        psum=psum+Nk*Ek*exp(-D*t*lamdak^2);
54. end
55. y = psum;
56. plot(t, y)
```

5. Code for Disk FRAP Model Using Neumann Boundary Condition

```
57. clear; clc; An=[ 3.8317  7.0156  10.1735  13.3237  16.4706  19.6159  22.7601  25.9037  29.0468
32.1897  35.3323  38.4748  41.6171  44.7593  47.9015  51.0435  54.1856  57.3275  60.4695
63.6114  66.7532  69.8951  73.0369  76.1787  79.3205  82.4623  85.6040  88.7458  91.8875
95.0292  98.1710  101.3127  104.4544  107.5961  110.7378  113.8794  117.0211  120.1628  123.3045
126.4461  129.5878  132.7295  135.8711  139.0128  142.1544  145.2961  148.4377  151.5794  154.7210
157.8627  161.0043  164.1459  167.2876  170.4292  173.5708  176.7125  179.8541  182.9957  186.1374
189.2790  192.4206  195.5622  198.7038  201.8455  204.9871  208.1287  211.2703  214.4119  217.5536
220.6952  223.8368  226.9784  230.1200  233.2616  236.4033  239.5449  242.6865  245.8281  248.9697
252.1113  255.2529  258.3945  261.5362  264.6778  267.8194  270.9610  274.1026  277.2442  280.3858
283.5274  286.6690  289.8106  292.9522  296.0938  299.2354  302.3771  305.5187  308.6603  311.8019
314.9435];
58.
59. t=[0:.1:5];
60. rho=5;
61. an=An/rho;
62. x=[0:.1:rho];
63. D=1;
64. K=.5;
65. r=1;
66. w=1;
67. Ci=1;
68. g_=(1-exp(-2*rho^2/r^2))*pi*r^2/2;
69. g=2*pi*exp(-x.^2/r/r)*g_;
70. SWk=0
71. for k=0:20
72.     gwk=exp(-2*k*x.^2/w/w);
```

```

73.     SWk=SWk+(-K)^k*trapz(x,x.*gwk)/factorial(k);
74. end
75. psum=0;
76. for n=1:30
77.     Rn=trapz(x,x.*g.*besselj(0,x.*an(n)));
78.     SWnk=0;
79.     for k=0:20
80.         gwk=exp(-2*k*x.^2/r/t);
81.         SWnk=SWnk+(-K)^k*trapz(x,x.*gwk.*besselj(0,x.*an(n)))/factorial(k);
82.     end
83.     psum=psum+SWnk*Rn*exp(-D*t*an(n)^2)/besselj(0,rho.*an(n))^2;
84. end
85.
86. y=Ci*(SWk + psum )*2/rho^2;
87. plot(t,y)

```

VITA

Jedidiah Koomson received his bachelors of science degree in actuarial science from Kwame Nkrumah University of Science & Technology in 2015. He was admitted into the graduate Mathematics program at Texas A&M University-Commerce in August 2016 and received his masters of science in mathematics in May 2018. He plans on joining the analytics industry, specifically to work in machine learning.

Mathematics Department
Texas A&M University-Commerce
Commerce, TX 75429
jedkoomson@outlook.com